nature structural & molecular biology

Structural basis for ESCRT-III protein autoinhibition

Monika Bajorek[1,2], Heidi L Schubert[1,2], John McCullough[1,2], Charles Langelier[1], Debra M Eckert[1], William-May B Stubblefield[1], Nathan T Uter[1], David G Myszka[1], Christopher P Hill[1] & Wesley I Sundquist[1]

Endosomal sorting complexes required for transport-III (ESCRT-III) subunits cycle between two states: soluble monomers and higher-order assemblies that bind and remodel membranes during endosomal vesicle formation, midbody abscission and enveloped virus budding. Here we show that the N-terminal core domains of increased sodium tolerance-1 (IST1) and charged multivesicular body protein-3 (CHMP3) form equivalent four-helix bundles, revealing that IST1 is a previously unrecognized ESCRT-III family member. IST1 and its ESCRT-III binding partner, CHMP1B, both form higher-order helical structures *in vitro,* and IST1-CHMP1 interactions are required for abscission. The IST1 and CHMP3 structures also reveal that equivalent downstream α5 helices can fold back against the core domains. Mutations within the CHMP3 core–α5 interface stimulate the protein's *in vitro* assembly and HIV-inhibition activities, indicating that dissociation of the autoinhibitory α5 helix from the core activates ESCRT-III proteins for assembly at membranes.

The endosomal sorting complexes required for transport (ESCRT) pathway functions in a series of important membrane-remodeling processes, including multivesicular body vesicle formation at endosomal membranes, enveloped virus budding from the plasma membrane and midbody abscission during cytokinesis (reviewed in refs. 1–4). In performing these functions, ESCRT components cycle between two different states: an inactive state, in which they are dispersed throughout the cytoplasm, and an active state, in which they are recruited to specific membranes by upstream adaptor proteins that induce tight membrane binding and component assembly. ESCRT recruitment and assembly ultimately lead to membrane fission, producing endosomal vesicles, budded viruses or daughter cells. The ESCRT pathway is therefore apparently a mobile machine that can be recruited to different membranes to help mediate membrane remodeling and fission.

Most of the approximately 30 proteins of the human ESCRT pathway function as components of one of five different complexes (termed the ESCRT-0–III and VPS4 complexes). These complexes are recruited sequentially to sites of action, with each successive complex recruiting and activating downstream complexes for membrane association and assembly[1–4]. Recent studies have revealed that subunits of the late-acting ESCRT-III complex can form rings, helical filaments and tubes *in vitro* and *in vivo*. Thus, ESCRT-III complexes may form 'collars' within the cytoplasm-filled necks of membrane vesicles and tubules that can constrict the neck and promote membrane fission[5–10]. Variants of this general model suggest that one specific subset of ESCRT-III proteins, those of the CHMP4/Snf7p (Snf7p is a yeast CHMP4 homolog) family, may create an encircling ring or spiral, and the other ESCRT-III proteins serve primarily to nucleate and cap the CHMP4 filament[8–10]. ESCRT-III proteins also recruit VPS4 ATPases and induce them to assemble into active complexes. Enzyme recruitment and activation are further promoted by the accessory factors IST1[11–14] and LIP5 (Vtalp in yeast)[1–4], both of which can bind ESCRT-III and VPS4 proteins. Once assembled, VPS4 uses the energy of ATP hydrolysis to release the assembled ESCRT-III machinery back into the cytoplasm, thereby allowing multiple rounds of membrane deformation and fission[10].

The 11 known human ESCRT-III–like proteins can be divided into seven different families, six of which (CHMP1–6) correspond to the six ESCRT-III–like proteins of *Saccharomyces cerevisiae*. Most ESCRT-III proteins can form both homo- and hetero-oligomers and can pair preferentially at membrane sites of action (for example, CHMP4–CHMP6 and CHMP2–CHMP3)[6,15]. ESCRT-III proteins vary considerably in primary sequence, but all share common N-terminal core domains of ~150 residues. The core domain of one ESCRT-III protein, $CHMP3_{8–183}$, has been crystallized and shown to form a four-helix bundle[16]. The longer first two helices form an extended hairpin, and the shorter two helices pack at the open end of the hairpin. Sequences located beyond the helical core have autoinhibitory activities, and there is now considerable biochemical and genetic evidence that these downstream sequences prevent premature membrane binding and assembly[6,16–21]. Downstream sequence elements also bind various late-acting ESCRT factors, including ALIX[22] and a series of microtubule-interacting and transport (MIT) domain–containing proteins and enzymes such as ubiquitin hydrolases (for example, AMSH and UBPY)[23,24], proteases (calpain 7)[25,26], ATPases (Spastin and VPS4 proteins)[21,27–30] and ATPase activators (LIP5 (Vtalp))[31–33]. Different ESCRT-III subunits have distinct binding partner specificities, helping to explain the need for so many different ESCRT-III proteins.

[1]Department of Biochemistry, University of Utah, Salt Lake City, Utah, USA. [2]These authors contributed equally to this work. Correspondence should be addressed to C.P.H. (chris@biochem.utah.edu) or W.I.S. (wes@biochem.utah.edu).

Received 4 January; accepted 19 May; published online 14 June 2009; doi:10.1038/nsmb.1621

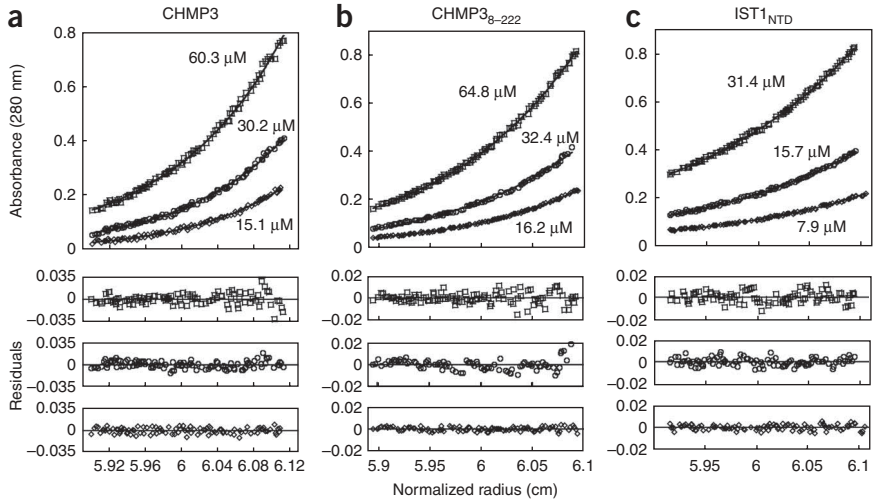

Figure 1 CHMP3, CHMP3$_{8–222}$ and IST1$_{NTD}$ are monomers in solution. (**a–c**) Equilibrium sedimentation distributions of recombinant CHMP3 (**a**), CHMP3$_{8–222}$ (**b**) and IST1$_{NTD}$ (**c**) (above), and residual differences (below), with data points shown in open symbols and the single species models shown as solid lines. Rotor speeds were 20,000 r.p.m. and the initial subunit protein concentrations are shown. Data sets were also collected at 24,000 r.p.m. (not shown) and all of the data were globally fit to single species models in which the molecular weights were allowed to float during the refinement. Estimated molecular weights were: CHMP3, 25,840 Da (molecular weight of the monomer ($MW_{monomer}$) = 25,267 Da, M_{obs}/M_{calc} = 1.02); CHMP3$_{8–222}$, 24,390 Da ($MW_{monomer}$ = 24,663 Da, M_{obs}/M_{calc} = 0.99); IST1$_{NTD}$, 20,520 Da ($MW_{monomer}$ = 21,791 Da, M_{obs}/M_{calc} = 0.94).

IST1 is a recently identified, late-acting ESCRT pathway factor that binds LIP5, VPS4 and CHMP1 (Did2p in yeast)[11–14]. The precise function(s) of IST1 are not well understood and, indeed, IST1 can exert both positive[11–14] and negative[12] effects on ESCRT pathway functions. Yeast Ist1p has synthetic interactions with the Vta1p–Vps60p (LIP5–CHMP5) complex in endosomal protein-sorting reactions, implying that Ist1p functions in the formation of multivesicular bodies (MVB), albeit in a non-essential role[12,13]. Human IST1 localizes to midbodies, and its depletion inhibits abscission but not HIV budding[11,14]. IST1 proteins therefore seem to have important roles in cytokinesis, auxiliary roles in endosomal protein sorting and no essential role in HIV budding. Biochemical and secondary-structure analyses indicate that IST1 is composed of a helical N-terminal domain (residues 1–189, here termed IST1$_{NTD}$, but also called the 'ELYC' domain after a conserved tetrapeptide sequence[12]), C-terminal MIT-interacting motifs (MIM) (residues 321–366) that can bind cooperatively to the MIT domains of VPS4 (refs. 11,14) and a central linker region that is predicted to lack persistent secondary structure (residues ~190–320)[11,14].

Extensive structural and biochemical analyses have revealed many of the relevant molecular interactions that allow different ESCRT components to associate with one another, with phosphatidylinositol-3-phosphate (PI(3)P)-containing membranes and with ubiquitylated protein cargoes[1–4]. In contrast, the mechanisms that regulate ESCRT pathway assembly and disassembly are much less well understood. Here we have determined crystal structures of the human IST1 and CHMP3 proteins. Furthermore, we have performed complementary biochemical analyses that characterize the functional importance of the IST1–CHMP1 binding interaction in cytokinesis, and we suggest how ESCRT-III proteins can switch between their inactive, soluble states and their active, membrane-bound assemblies.

RESULTS

Characterization of recombinant CHMP3 and IST1 proteins

We developed methods for expressing and purifying recombinant human IST1 and CHMP3 proteins for structural and biochemical studies. Full-length CHMP3 and an N-terminally truncated construct (CHMP3$_{8–222}$) were both monomeric in solution, as analyzed by equilibrium sedimentation (**Fig. 1a**,**b**), in good agreement with a previous report[16]. Full-length IST1 was also monomeric under high-ionic-strength conditions (>300 mM NaCl)[11], but aggregated at lower ionic strength. The purified N-terminal domain of IST1 (IST1$_{NTD}$) behaved similarly to the full-length protein in that it was also monomeric under high-ionic-strength conditions (**Fig. 1c**) and insoluble in lower-ionic-strength solutions. This construct was particularly amenable for structural and biochemical studies, presumably because it lacked the proline-rich linker region present in the full-length protein.

Crystal structures of IST1$_{NTD}$

We crystallized IST1$_{NTD}$ under high-ionic-strength conditions and determined the structure in space groups $P2_1$ (1.8-Å resolution) and $P4_32_12$ (2.6-Å resolution) (**Table 1** and **Supplementary Fig. 1**). The structures were similar, and the higher-resolution $P2_1$ structure is described here. IST1$_{NTD}$ is composed of eight helices that pack to create a flat, elongated structure, with overall dimensions of 21 × 30 × 60 Å (**Fig. 2a**). The two longest helices, α1 and α2, form a helical hairpin that packs against the smaller α3 and α4 helices to create an asymmetric four-helix bundle (termed the 'core'). Beyond the core, the segment between helices α4 and α5 forms a flap that tracks along the length of the molecule, packing against the α2-α3 edge. The flap contains two short helices, designated αA and αB to maintain a consistent numbering scheme for conserved ESCRT-III helices. Helix α5 packs perpendicularly across helices α1 and α2 near the closed end of the hairpin and is termed the 'autoinhibitory helix'. A final turn takes the polypeptide across the hairpin loop and into α6, which projects away from the core. This helix was seen in only the $P2_1$ crystal form, where it is stabilized by lattice contacts. As discussed below, the IST1$_{NTD}$ structure seems to represent a closed, autoinhibited ESCRT-III conformation in which the flap and autoinhibitory helix fold against the core to prevent higher-order interactions.

IST1$_{NTD}$ bears an unexpected resemblance to the published CHMP3$_{8–183}$ structure[16] (**Fig. 2a–c**), and the four helices of the IST1$_{NTD}$ core superimpose with the first four helices of CHMP3 with an r.m.s. deviation of 2.4 Å (128 Cα positions). Muziol *et al.* noted that the α1 edge of CHMP3 is distinctly cationic and proposed that this surface binds membranes[16]. The equivalent IST1 surface is also basic, although the α3-α4 face is even more so (**Fig. 2d–f**).

In addition to their similar core structures, the autoinhibitory α5 helices of CHMP3$_{8–183}$ and IST1$_{NTD}$ sit in equivalent positions (**Fig. 2a–c**, α5, orange). Thus, all of the ordered helices in the CHMP3$_{8–183}$ structure have analogs in IST1$_{NTD}$. However, the assigned connectivity of the autoinhibitory helices differ between the two structures because this helix is connected in *cis* to the IST1$_{NTD}$

Table 1 $IST1_{NTD}$ and CHMP3 crystallographic statistics

	$IST1_{NTD}$: Native 1	$IST1_{NTD}$: Peak 1	$IST1_{NTD}$: Inflection 1	$IST1_{NTD}$: Remote 1	$IST1_{NTD}$: Native 2	$CHMP3_{8–222}$	$CHMP3_{1–150}$
Data collection							
Space group	$P4_32_12$	$P4_32_12$	$P4_32_12$	$P4_32_12$	$P2_1$	$P2_1$	$P6_1$
Cell dimensions							
a, *b*, *c* (Å)	57.2, 57.2, 157.2	57.6, 57.6, 157.1	57.6, 57.6, 157.2	57.7, 57.7, 157.3	29.3, 92.4, 33.25	36.5, 131.5, 48.5	111.5, 111.5, 30.6
α, β, γ (°)	90.0, 90.0, 90.0	90.0, 90.0, 90.0	90.0, 90.0, 90.0	90.0, 90.0, 90.0	90.0, 97.0, 90.0	90.0, 108.1, 90.0	90.0, 90.0, 120.0
Resolution (Å)[a]	40–2.6 (2.7-2.6)	40–3.4 (3.5–3.4)	40–3.4 (3.5–3.4)	40–3.4 (3.5–3.4)	50–1.80 (1.86–1.80)	50–4.0 (4.14–4.0)	25–3.7 (3.83–3.7)
R_{sym}	6.8 (34)	7.5 (16)	5.9 (15)	6.5 (14)	5.8 (15)	0.16 (15)	0.063 (55)
$I/\sigma I$	13.5 (1.7)	23.9 (5.0)	24.3 (4.4)	24.4 (3.8)	19.2 (4.6)	9.3 (2.9)	18.4 (2.2)
Completeness (%)	97.7 (88.3)	88.5 (56.5)	87.7 (55.4)	83.4 (42.8)	97.2 (79.1)	78.7 (43.9)	99.2 (96.8)
Redundancy	3.8 (2.8)	6.7 (5.8)	3.9 (3.6)	3.9 (4.0)	3.1 (1.8)	4.0 (2.8)	3.2 (3.1)
Refinement							
Resolution (Å)	40–2.6				50–1.80	38–4.0	24–3.7
No. reflections	7,968				15,213	2,936	2,449
R_{work} / R_{free} (%)	25.9 / 29.8				19.5 / 24.7	37	41
No. atoms							
Protein	1,438				1,558	2,274	973
Water	35				163	0	0
B-factors (Å^2)							
Protein	87.2				26.0	n/a[b]	n/a[b]
Water	69.0				39.4	n/a[b]	n/a[b]
r.m.s. deviations							
Bond lengths (Å)	0.0007				0.011	n/a[b]	n/a[b]
Bond angles (°)	1.2				1.3	n/a[b]	n/a[b]

[a]Values in parentheses are for the highest-resolution shell. [b]*B*-factors and individual atomic parameters were not refined and are unchanged from the molecular replacement model.

core via the flap segment, whereas it was assigned to an adjacent molecule in the $CHMP3_{8–183}$ lattice[16]. Muziol *et al.* noted, however, that the $CHMP3_{8–183}$ connectivity could not be defined unambiguously owing to a lack of visible electron density for the flap region[16]. We therefore speculate that the $CHMP3_{8–183}$ connectivity may actually match that of $IST1_{NTD}$ and that the $CHMP3_{8–183}$ structure may also represent a closed conformation.

Crystal structures of CHMP3

The $CHMP3_{8–183}$ construct lacked the final 39 CHMP3 residues, which may have favored an open conformation[16]. We therefore attempted to remove this ambiguity by crystallizing both the full-length monomeric $CHMP3_{1–222}$ protein and a slightly truncated $CHMP3_{8–222}$ protein. Both proteins crystallized isomorphously in space group $P2_1$, but $CHMP3_{8–222}$ diffracted to slightly higher resolution (4.0 Å), and this structure is therefore reported (**Fig. 2c** and **Table 1**). We determined the $CHMP3_{8–222}$ structure by molecular replacement, using the core of $CHMP3_{8–183}$ as a search model, and then subjected the structure to rigid body refinement. Discernible features beyond the search model were limited, but the structure solution is supported by the molecular replacement statistics (see Online Methods) and by unbiased electron density maps (**Supplementary Fig. 2**). In addition to the four core helices, density for the autoinhibitory helix was evident in unbiased electron density maps, particularly for one of the two independent molecules in the asymmetric unit (**Supplementary Fig. 2c,d**). Although the connectivity between α4 and α5 was not defined by experimental electron density,

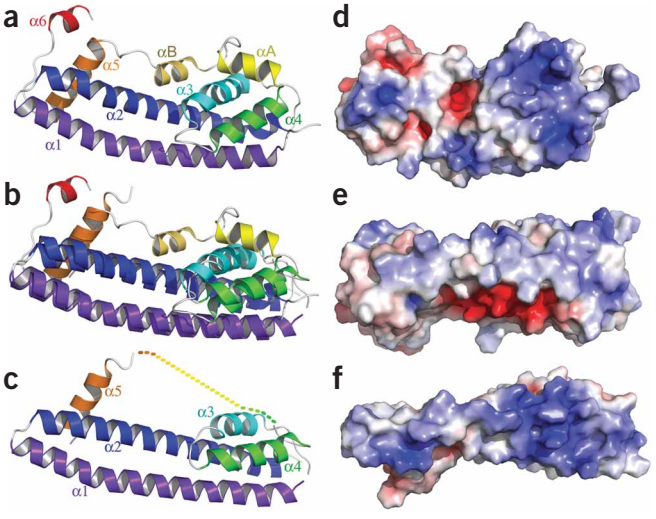

Figure 2 Structures of $IST1_{NTD}$ and CHMP3. (**a**) Ribbon diagram and helix-labeling scheme for $IST1_{NTD}$. (**b**) Overlay of the ordered regions of $IST1_{NTD}$ and $CHMP3_{8–183}$. (**c**) Ribbon diagram of $CHMP3_{8–222}$. (**d**) Space-filling model of $IST1_{NTD}$, color coded to show the surface charge distribution (blue, basic; red, acidic; ±7 kV)[35] (created using PyMOL (http://pymol.sourceforge.net)). The molecule is shown in the same orientation as in **a**. (**e**) Same as **d** with the view toward α1. Figure generated from **d** by rotation about the horizontal so that the bottom edge of **d** faces the viewer. (**f**) Space-filling model of $CHMP3_{8–222}$ shown in an equivalent orientation to the view of $IST1_{NTD}$ shown in **e**, emphasizing the basicity of the α1 surface of CHMP3 (ref. 16).

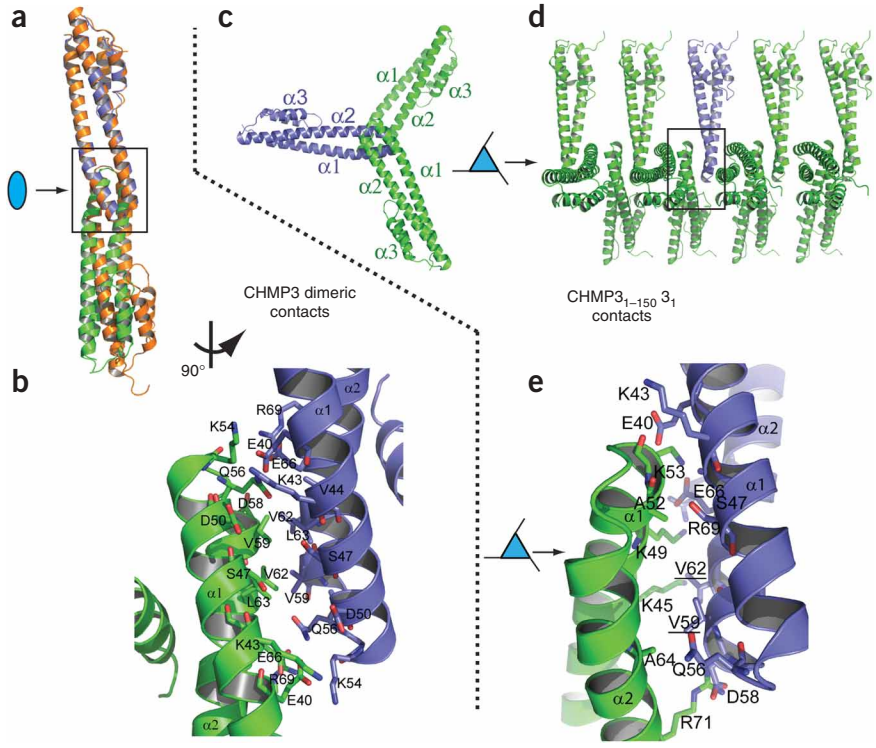

Figure 3 CHMP3 crystal packing interactions. (**a**) Overlay of the cores of the tip-to-tip dimers in the crystal lattices of CHMP3$_{8–183}$ (orange)[16] and CHMP3$_{8–222}$ (blue and green). The upper subunits were aligned, and the lower subunits diverge owing to small differences in their tip-to-tip interfaces. (**b**) Detailed expansion of the boxed region of CHMP3$_{8–222}$ shown in **a**. Most side chains conformations are shown as defined in the CHMP3$_{8–183}$ search model, with some minor adjustments to avoid clashes. Precise description of these side chain conformations is not possible at current resolutions. (**c**) Subunit packing down the 3_1 screw axis of the CHMP3$_{1–150}$ crystal lattice, with a single CHMP3$_{1–150}$ molecule highlighted in blue. (**d**) Same assembly as in **c** but viewed perpendicularly to the 3_1 screw axis. (**e**) Detailed expansion of the boxed area shown in **d**. As in **b**, most side chains conformations are shown as defined in the CHMP3$_{8–183}$ search model, with some minor adjustments to avoid clashes.

α5 seems to sit in the same position in both the CHMP3$_{8–183}$ and the CHMP3$_{8–222}$ structures, despite different crystal packing interactions in the two lattices. We have connected α4 and α5 in *cis* rather than in *trans* to create a structure with the same topology as IST1$_{NTD}$, and this assignment is consistent with biochemical analyses described below.

Finally, we reasoned that a construct corresponding to the CHMP3 core alone could not adopt an autoinhibited conformation and might therefore reveal authentic protein-protein interactions used for ESCRT-III assembly. We crystallized the CHMP3 core construct (CHMP3$_{1–150}$) in space group $P6_1$ and solved the structure by molecular replacement (3.7-Å resolution; **Table 1** and **Supplementary Fig. 2b**). As expected, the CHMP3$_{1–150}$ core was similar to the cores of the other CHMP3 and IST1$_{NTD}$ structures, although, as described below, the lattice interactions were unique.

Crystal packing interactions

We analyzed lattice contacts in the different IST1 and CHMP3 crystal structures to determine whether they were strong candidates for authentic interactions used in ESCRT-III protein assembly (see **Supplementary Figure 3** for a complete catalog of the different lattice interactions). Overall, there are no compelling reasons to believe that any of the various crystal contacts represent authentic assembly interfaces. Moreover, both of our CHMP3 structures lacked the 'side-to-side' dimer interface seen in the CHMP3$_{8–183}$ structure[16] and postulated as a possible ESCRT-III assembly interface[6,7].

Two of the new CHMP3 interfaces merit comment because they are mediated by a conserved, exposed hydrophobic surface on the closed 'tip' of the α1-α2 hairpin. In the CHMP$_{8–222}$ structure, two adjacent molecules associate through a small (359 Å^2) two-fold symmetric 'tip-to-tip' dimer interface (**Fig. 3a**,**b**). A similar tip-to-tip interface was also present in the CHMP3$_{8–183}$ lattice[16], and this is the only interface that has been seen in more than one crystal form.

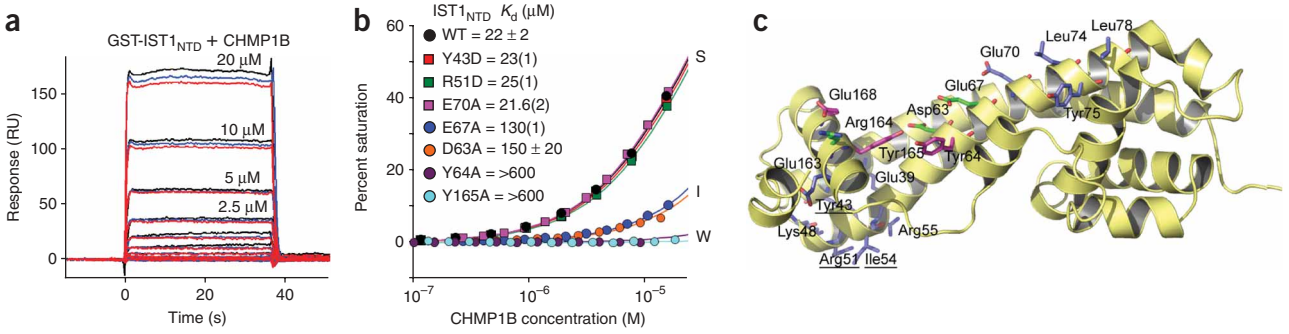

Figure 4 Mutational analyses of IST1–CHMP1B interactions. (**a**) Sensorgrams showing different concentrations of purified CHMP1B binding to immobilized GST-IST1$_{NTD}$. Triplicate measurements in response units (RU) are shown for each CHMP1B concentration. (**b**) Representative biosensor binding isotherms showing CHMP1B binding to wild-type (WT) and mutant GST-IST1$_{NTD}$ proteins with strong (S), intermediate (I) and weak (W) binding affinities. IST1$_{NTD}$ mutations and estimated dissociation constants are given in the inset. Errors represent either s.d. from multiple independent measurements ($n \geq 3$) or s.d. derived from single isotherms measured in triplicate (values in parentheses report the s.d. in the final digit of the measurement). (**c**) Ribbon diagram showing the location of all IST1$_{NTD}$ mutations tested for CHMP1B binding. Mutated residues are shown explicitly, and the binding affinities of the mutant proteins are color coded as follows: blue, strong (S) binding (binding affinities within 1.5-fold of wild-type IST1$_{NTD}$); green, intermediate (I) binding (binding affinity reduced 1.5-fold to 8-fold); magenta, weak (W) binding (binding affinity reduced ≥8-fold).

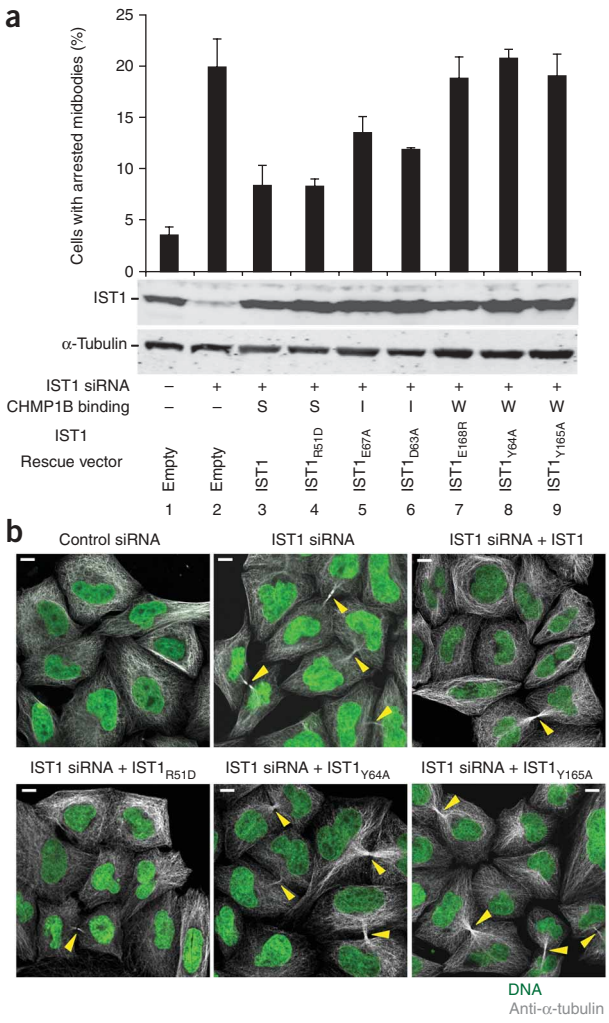

Figure 5 Requirement for IST1–CHMP1 interactions during abscission. (**a**) Above, quantified abscission defects as reflected in the percentages of HeLa M cells with visible midbodies following siRNA treatment to deplete endogenous IST1 (lanes 2–9) and rescue with an empty vector control (lane 2, negative control) or with vectors expressing wild-type IST1 (lane 3, positive control) or the designated IST1 mutants (lanes 4–9). Untreated cells are shown in lane 1. Error bars show s.d. from three independent repetitions of the experiment. Middle, western blot (anti-IST1) showing levels of soluble endogenous IST1 (lanes 1 and 2) or exogenously expressed IST1 proteins (lanes 3–9). Below, a western blot (anti–α-tubulin) showing expression levels of endogenous α-tubulin (loading control). CHMP1B binding phenotypes of the different IST1 proteins are shown below: strong (S), intermediate (I) or weak (W). (**b**) Immunofluorescence images showing the midbody phenotypes of cells from a designated subset of the experiments from **a**. Microtubules (anti–α-tubulin, gray) and nuclei (SYTOX Green) were stained for reference, and yellow arrowheads highlight midbodies. Scale bars, 10 μm.

A different type of tip-to-tip interaction is present in the $CHMP3_{1–150}$ lattice. In this case, the interaction lacks two-fold rotational symmetry and instead follows a crystallographic 3_1 screw axis that creates an infinite $CHMP3_{1–150}$ filament with interfaces on both sides of the tip (**Fig. 3c–e**). The yeast homolog of CHMP3 (Vps24p) can assemble into three-stranded filaments *in vitro*[7], although the relationship between the Vps24p filaments and the crystallographic CHMP3 filaments remains to be determined. In summary, the crystal packing interactions in our IST1 and CHMP3 structures do not obviously correspond to authentic biological interfaces, but do reinforce the idea that the exposed hydrophobic surface located at the tip of the helix 1–helix 2 loop is a preferred site for protein-protein interactions[6,7,16].

$IST1_{NTD}$ binds CHMP1 proteins

Many ESCRT-III proteins bind one another, and previous studies have shown that the N-terminal domain of IST1 binds preferentially to the C-terminal region of the CHMP1 subset of ESCRT-III proteins[11–14]. To map the IST1 binding surface more precisely, we created an ensemble of IST1 proteins with point mutations at conserved, surface-exposed residues and tested them for CHMP1A and CHMP1B interactions using: (i) immunoprecipitation reactions in 293T cells (not shown), (ii) glutathione *S*-transferase (GST) pull-down experiments with recombinant proteins (not shown) and (iii) biosensor binding experiments in which pure recombinant CHMP1B bound immobilized GST-$IST1_{NTD}$ (**Fig. 4**).

CHMP1B bound wild-type $IST1_{NTD}$ with an estimated dissociation constant of 22 ± 2 μM (**Fig. 4a**,**b**). CHMP1B binding was unaltered by most mutations tested, including mutations within the closed tip of the α1-α2 hairpin (for example, E39A, Y43D, K48D, R51D, I54D and R55D) and in the $IST1_{NTD}$ surface that corresponded to the side-to-side dimer interface seen in the crystal structure of $CHMP3_{8–183}$ and included the signature 73-ELYCEL-78 motif (for example, E70A, L74R, Y75A and L78R). However, one mutation along helix 2 (E67A) reduced CHMP1B binding in the immunoprecipitation and pull-down experiments and lowered the CHMP1B binding affinity six-fold in the biosensor binding assay, suggesting that this residue contributed to the CHMP1B binding site. We therefore tested mutations in adjacent surface-exposed residues to identify the CHMP1B binding site more precisely. Three IST1 mutants bound CHMP1B weakly (reductions in affinity of more than eight-fold; $IST1_{Y64D}$, $IST1_{Y165A}$ and $IST1_{E168R}$), three bound CHMP1B with intermediate affinities (two- to eight-fold reductions; $IST1_{D63A}$, $IST1_{E67A}$ and $IST1_{R164D}$) and one still bound strongly to CHMP1B ($IST1_{E163R}$; data not shown).

Given the proximity of the apparent CHMP1B binding site to the IST1 autoinhibitory helix α5, we also tested the effects of a series of IST1 mutations predicted to destabilize the α5-core interface (V56D, I60D, L166D and I169D). All of these IST1 mutations blocked CHMP1B binding entirely (data not shown), indicating that CHMP1B binds the closed conformation of $IST1_{NTD}$ seen in the crystal structures. As summarized in **Figure 4c**, mutations that inhibited CHMP1B binding clustered within or near a groove created by packing of autoinhibitory helix α5 against core helix α2. The groove features a pair of exposed tyrosine residues (Tyr64 and Tyr165) that probably contribute to CHMP1B binding.

The IST1–CHMP1B interactions function in cytokinesis

To determine whether CHMP1 binding was necessary for IST1 cytokinesis function(s), we tested whether IST1 mutations that impaired CHMP1B binding also inhibited abscission. Depletion of endogenous IST1 increased the percentage of HeLa cells with visible midbodies from 4 ± 1% to 20 ± 3% (**Fig. 5a**, compare lanes 1 and 2, and **Fig. 5b**, compare image above left with image above middle), and this midbody arrest defect was largely (but not entirely) rescued by re-expression of a wild-type, small interfering RNA (siRNA)-resistant IST1 construct (8 ± 2%; **Fig. 5a**, lane 3, and **Fig. 5b**, above right)[11]. Midbody arrest was also corrected by an IST1 protein with a mutation in the tip of the α1-α2 hairpin that retained strong (S) CHMP1B binding ($IST1_{R51D}$, 8 ± 1%; **Fig. 5a**, lane 4,

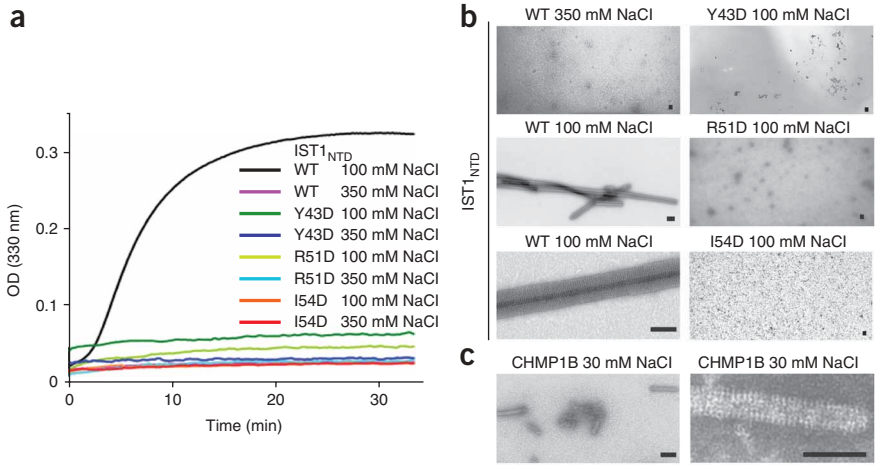

Figure 6 $IST1_{NTD}$ and CHMP1B tube assembly. (**a**) Assembly of wild-type (WT) $IST1_{NTD}$ or three different $IST1_{NTD}$ mutants with the designated amino acid substitutions at the tip of the α1-α2 hairpin (mutated residues are underlined in **Figure 4c**). $IST1_{NTD}$ proteins were diluted from concentrated protein stocks in high-salt buffers to final concentrations of 62 μM. Salt concentrations in the assembly buffers are provided in the inset key and protein assembly was followed by light scattering at 330 nm. (**b**) TEM images of a subset of the wild-type and mutant $IST1_{NTD}$ assembly reactions from **a**. Note that $IST1_{NTD}$ assembled only under low-salt conditions (compare upper and middle left images) and that $IST1_{NTD}$ proteins with different point mutations at the tip of the α1-α2 hairpin did not assemble in either high-salt (not shown) or low-salt conditions (right). An expanded view of a single $IST1_{NTD}$ tube is shown in the lower left image. Scale bars, 500 nm. (**c**) TEM images of CHMP1B tubes assembled under low-salt conditions. A field of tubes is shown at left and an expanded view of a single CHMP1B tube is shown at right. Scale bars, 500 nm.

and **Fig. 5b**, below left). In contrast, three weakly binding IST1 mutants failed to rescue midbody arrest (18–21%; **Fig. 5a**, lanes 7–9, and **Fig. 5b**, images below middle and below right). Point mutations within the α5-core interface that blocked CHMP1B binding also blocked rescue of the midbody arrest defect. However, these mutant proteins partitioned almost exclusively into the insoluble, membrane-bound cellular fractions, and their failure to support abscission may therefore reflect either aberrant CHMP1 binding or IST1 protein mislocalization (**Supplementary Fig. 4 and Supplementary Discussion**). Finally, two IST1 mutants with intermediate (I) CHMP1B binding affinities rescued midbody arrest to an intermediate extent (12–13%; **Fig. 5a**, lanes 5 and 6). Hence, there was an excellent correlation between the ability of different IST1 constructs to bind CHMP1B *in vitro* and to function in abscission, indicating that CHMP1 binding is required for IST1 abscission function(s).

$IST1_{NTD}$ and CHMP1B form homopolymeric helices *in vitro*

CHMP3 can co-polymerize with truncated CHMP2A proteins to form helical tubes 50 nm in diameter *in vitro*[6]. As noted above, both IST1 and $IST1_{NTD}$ became insoluble under low-ionic-strength conditions, and we therefore tested whether these proteins assembled into regular structures. We initially surveyed assembly conditions using light scattering to follow complex formation. Monomeric $IST1_{NTD}$ spontaneously polymerized into high-molecular-weight complexes that strongly scattered light at 330 nm when the protein was diluted from a high-salt buffer (350 mM NaCl) into a low-salt buffer (100 mM NaCl) (**Fig. 6a**). In contrast, $IST1_{NTD}$ did not scatter light when diluted into an otherwise equivalent high-salt buffer (350 mM NaCl).

EM analyses revealed that the light-scattering $IST1_{NTD}$ assemblies were large tubular structures with diameters of ~700 nm (**Fig. 6b**, lower left images). The tubes seemed to be open along one edge and may therefore be curled sheets rather than fully closed

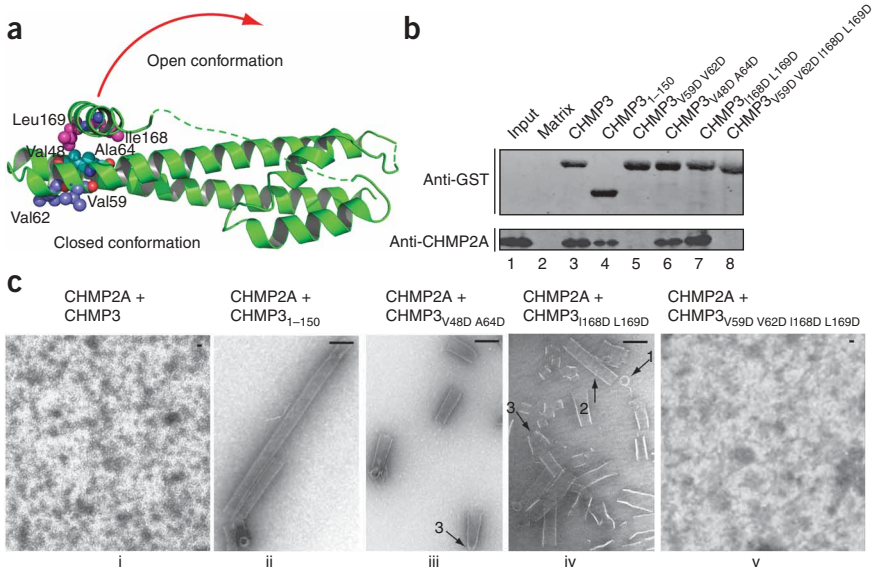

Figure 7 CHMP3 activation *in vitro*. (**a**) Ribbon diagram showing the locations of mutated CHMP3 residues at the tip of the α1-α2 hairpin (purple) and activating mutations on either side of the interface between the core α2 helix (cyan) and the autoinhibitory α5 helix (magenta). The red arrow suggests how the closed CHMP3 conformation might convert into an open conformation by dissociation of the autoinhibitory α5 helix from the core. (**b**) GST pull-down analyses of the binary CHMP3–CHMP2A interaction. Pure recombinant CHMP2A (below, anti-CHMP2A) was tested for binding to a glutathione-Sepharose matrix (lane 2, negative control) or to immobilized wild-type (lane 3) or mutant GST-CHMP3 proteins (lanes 4–8). Both proteins were detected by western blotting, and input CHMP2A (0.3%) is shown in lane 1 for reference. (**c**) EM analyses of helical CHMP3–CHMP2A assembly. Different panels show assemblies formed by 1:1 mixtures of CHMP2A with: full length, wild-type CHMP3 (i, negative control, no assembly), $CHMP3_{1–150}$ core domain (ii, positive control), activated $CHMP3_{V48D\ A64D}$ (iii), activated $CHMP3_{I168D\ L169D}$ (iv), and activated and tip mutant $CHMP3_{V59D\ V62D\ I168D\ L169D}$ (v, no assemblies). Arrows highlight rings (1), tubes (2) and cones, or tapered tubes (3). Scale bars, 100 nm.

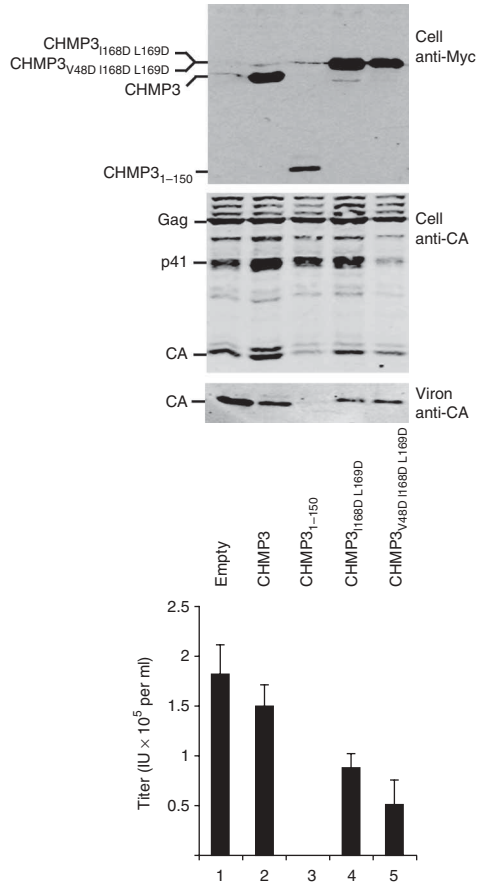

Figure 8 CHMP3 activation *in vivo*. HIV-1 vector expression and release upon co-expression with an empty vector (negative control, lane 1), or with vectors expressing wild-type CHMP3 (negative control, lane 2), a $CHMP3_{1–150}$ protein lacking the entire autoinhibitory region (positive control, lane 3), proteins with activating mutations in the α5-core interface: $CHMP3_{I168D\ L169D}$ (lane 4) and $CHMP3_{V48D\ 168D\ L169D}$ (lane 5). The two uppermost western blots show cellular expression levels of CHMP3-Myc proteins (panel 1, anti-Myc) and of the viral Gag protein and its p41 and CA-processing products (panel 2, anti-CA). The western blot below shows levels of released, virion-associated CA proteins. The graph shows the infectious titers of HIV-1 vectors released under the different conditions (infectious units (IU) per ml; error bars show s.d. in multiple titer measurements, $n \geq 4$).

helices. Lattice lines were evident in some assemblies, and the clearest lattice spacing was ~440 Å, which presumably represents a supermolecular spacing because the maximal length of a single $IST1_{NTD}$ molecule is only ~60 Å. As noted above, CHMP3 interactions can be mediated by various different kinds of tip-to-tip interactions[6,7] (**Fig. 3**). A series of three point mutations in the analogous IST1 surface (Y43D, R51D and I54D) also inhibited $IST1_{NTD}$ polymerization (**Fig. 6a,b**, right) (see **Supplementary Fig. 5** for ESCRT-III protein alignments). $IST1_{NTD}$ assembly therefore probably also requires some type of tip-to-tip interaction.

We also attempted to test whether $IST1_{NTD}$ and CHMP1B could co-polymerize in a manner similar to the $CHMP2A_{9–161}$–CHMP3 pair[6]. However, controls for these experiments revealed that pure recombinant CHMP1B alone polymerized into helical tubes when diluted into low-salt buffers, even in the absence of $IST1_{NTD}$ (**Fig. 6c**). CHMP1B tubes were of intermediate size (~230 nm in diameter), seemed to be fully closed and had visible lattice spacing of ~420 Å, similar to the lattice spacing in the $IST1_{NTD}$ tubes. Thus, both $IST1_{NTD}$ and CHMP1B, as for CHMP2A–CHMP3 (ref. 6), form tubular structures *in vitro*, and the ability to assemble into helical tubes therefore seems to be a property common to many ESCRT-III core domains. However, the IST1 and CHMP1B tubes were homopolymeric, and they were substantially larger than those formed by CHMP2A–CHMP3 heteropolymers[6].

CHMP3 α1-α2 hairpin tip binds CHMP2A

As with the IST1–CHMP1 pair, CHMP2A and CHMP3 bind one another preferentially. To investigate this interaction further, we used GST pull-down assays to test for binary interactions between CHMP2A and GST-CHMP3 (**Fig. 7a,b**). We performed these experiments at low protein concentrations where higher-order assemblies were not detectable (35 μM CHMP2A, ~7 μM GST-CHMP3). CHMP2A protein bound GST-CHMP3 (**Fig. 7b**, lane 3) but did not bind a matrix control (lane 2). CHMP2A also bound the truncated $GST\text{-}CHMP3_{1–150}$ protein (lane 4), indicating that CHMP2A interacted with the CHMP3 core and that the binary interaction was not strongly affected by removal of the terminal CHMP3 autoinhibitory sequences. In contrast, a double point mutation (V59D V62D) that disrupted the exposed hydrophobic surface on one side of the tip of the CHMP3 α1- α2 hairpin eliminated CHMP2A binding (lane 5). These data suggest that CHMP2A and CHMP3 interact through a tip-to-tip interaction and demonstrate that the binary CHMP2A–CHMP3 and IST1–CHMP1B pairs interact via different binding surfaces, and therefore form structurally distinct complexes.

Autoinhibitory helix inhibits CHMP3 polymerization

Comparative analyses of the $IST1_{NTD}$, $CHMP3_{8–183}$ and $CHMP3_{8–222}$ structures suggested a model for ESCRT-III autoinhibition in which the α5 helix and flap elements fold back against the protein core to prevent higher-order assembly. We tested this idea by introducing destabilizing mutations within the α5-core interface of the full-length CHMP3 protein and testing their effects on CHMP2A co-assembly. Although the full-length CHMP2A and CHMP3 proteins bind one another, these two proteins do not readily form higher-order helical assemblies[6] (**Fig. 7c,i**). In contrast, a $CHMP3_{1–150}$ protein that lacked the flap and autoinhibitory helix readily co-polymerized with CHMP2A to form long, regular helical tubes (**Fig. 7c,ii**, positive control). As CHMP2A forms binary complexes with both CHMP3 and $CHMP3_{1–150}$, these experiments imply that CHMP3 residues 151–222 inhibit additional interaction(s) required for higher-order assembly.

To examine the mechanism of CHMP3 autoinhibition, we mixed full-length CHMP2A with full-length CHMP3 proteins that contained mutations on either side of the core-α5 interface ($CHMP3_{V48D\ A64D}$ and $CHMP3_{I168D\ L169D}$, **Fig. 7a**). Both sets of mutations activated CHMP3 for assembly, as reflected in the formation of numerous rings, tubes and cones (**Fig. 7c,iii,iv**). The tubes were similar in diameter to those formed in the CHMP2A–$CHMP3_{1–150}$ control reaction (~50 nm) but were typically shorter, possibly because the point mutations activated CHMP3 proteins less fully than removal of the entire autoinhibitory region.

We also tested whether the binary CHMP2A–CHMP3 interface detected at low protein concentrations was required for higher-order assembly. As expected, mutations on either side of the CHMP3 autoinhibitory interface did not substantially affect CHMP2A binding to GST-CHMP3 ($CHMP3_{V48D\ A64D}$ and $CHMP3_{I168D\ L169D}$; **Fig. 7b**, lanes 6 and 7). However, a CHMP3 protein carrying mutations in both the tip and autoinhibitory interfaces ($CHMP3_{V59D\ V62D\ I168D\ L169D}$) could neither bind CHMP2A in the GST pull-down assay (**Fig. 7b**, lane 8) nor assemble into helical tubes (**Fig. 7c,v**). These experiments

imply that tip-to-tip interactions contribute to CHMP2–CHMP3 co-assembly, in good agreement with a previous study[6].

Mutations in the autoinhibitory helix activate CHMP3 *in vivo*

Although co-expression of full-length CHMP3 has only minimal effects on HIV-1 budding, truncated CHMP3 constructs lacking the C-terminal autoinhibitory elements potently inhibit virus budding, presumably because the activated protein sequesters itself and other ESCRT-III proteins on cellular membranes[20]. Inhibition of HIV release therefore provides a sensitive assay for CHMP3 activation *in vivo*. We used this system to examine whether mutations in the α5-core interface also activate CHMP3 *in vivo*. Overexpression of full-length CHMP3 together with an HIV-1 vector system in 293T cells had little effect on the release of viral particles, as measured by the levels of virion-associated CA proteins released (**Fig. 8**, image 3, compare lanes 1 and 2) or by viral titers (**Fig. 8**, image 4, compare lanes 1 and 2). In contrast, HIV release and infectivity were potently inhibited by co-expression of a CHMP3 protein that lacked the autoinhibitory region entirely ($CHMP3_{1–150}$, positive control, compare lanes 2 and 3, showing a >250-fold infectivity reduction). In the actual experiment, two different CHMP3 proteins with point mutations within the α5-core interface ($CHMP3_{I168D\ L169D}$ and $CHMP3_{V48D\ I168D\ L169D}$) reduced HIV vector release and infectivity by 1.7-fold and 3-fold, respectively (compare lanes 4 and 5 to lane 2). Western blots confirmed that the full-length CHMP3 proteins and viral Gag proteins and proteolytic processing products were expressed at similar levels (images 1 and 2, respectively). Thus, point mutations in the α5-core interface enhanced the ability of CHMP3 proteins to inhibit HIV-1 budding *in vivo*, although this enhancement was much weaker than that seen upon deletion of the entire autoinhibitory region. We presume that the weaker effects seen for the point mutants reflects either incomplete activation and/or their ability to interact with VPS4, which will reduce their propensity to become 'trapped' on membranes, as compared to $CHMP3_{1–150}$ (which lacks a terminal VPS4 binding site).

DISCUSSION

Our studies have unexpectedly revealed that the N-terminal domain of IST1 contains an asymmetric four-helix bundle that closely resembles the core of the ESCRT-III protein CHMP3 (**Fig. 2**). As is true for other ESCRT-III proteins, IST1 (i) localizes to midbodies and functions in cytokinesis[11,14] and MVB vesicle sorting[12,13], (ii) binds preferentially to another subset of ESCRT-III proteins (the CHMP1 proteins)[11–14], (iii) contains MIM elements near its C terminus that can bind VPS4 and LIP5 MIT domains[11,14] and (iv) can self-assemble into tubular structures *in vitro* (**Fig. 6**). Thus, despite its larger size and primary sequence divergence, IST1 is an ESCRT-III protein family member.

Despite these similarities, there are also important differences between IST1 and CHMP3, particularly in the binary interactions that they make with their CHMP1 and CHMP2 binding partners. Our mutational analyses mapped the CHMP1 binding site to a groove formed by the autoinhibitory α5 helix and the core α2 helix of $IST1_{NTD}$ (**Fig. 4**). CHMP1B binding was also inhibited by mutations expected to favor the (hypothetical) open $IST1_{NTD}$ conformation, implying that CHMP1 binds the closed conformation seen in our $IST1_{NTD}$ crystal structures (**Fig. 2**). IST1 mutations that blocked CHMP1B binding also prevented IST1 from functioning in abscission, implying that these two proteins must act together during this final stage of cytokinesis (**Fig. 5**). In contrast, binary interactions between CHMP2 and CHMP3 were not inhibited by mutations that displaced or even removed the α5 helix entirely (**Fig. 7**). This interaction was sensitive to mutations at the tip of the α1-α2 hairpin, however, suggesting that, unlike IST1 and CHMP1B, CHMP2 and CHMP3 probably interact through some sort of a tip-to-tip interaction (**Fig. 7**).

In vitro assemblies formed by ESCRT-III proteins include filaments, rings, cones, curled sheets and tubes[6,7] (**Figs. 6b,c** and **7c**). At present, we do not know which (if any) of these different *in vitro* assemblies mimic different ESCRT-III assemblies formed *in vivo*. As noted previously[5–7], however, filaments, rings and/or tubes could correspond to 'collars' within the necks of budding particles, and tapered tubes or spiraling cones could provide a mechanism for closing the neck during budding[6] (**Fig. 7c**, structure type 3). Although the precise molecular interactions that mediate higher-order ESCRT-III assembly remain to be determined, both $IST1_{NTD}$ and CHMP2–CHMP3 assemblies are inhibited by point mutations within the conserved, exposed hydrophobic surface located at the tip of the α1-α2 hairpin (**Figs. 6b** and **7c**), suggesting that some type of tip-mediated interface forms within both assemblies. Two distinct types of homopolymeric ESCRT-III tip-to-tip interactions have now been seen crystallographically[16] (**Fig. 3**), and a third type was inferred from cryo-EM studies of helical yeast Vps24 (CHMP3) assemblies[7]. Thus, the conserved hydrophobic surface at the tip of ESCRT-III proteins is a preferred interaction site, although it is not yet clear which, if any, of the tip-to-tip interactions characterized to date represent biologically relevant interactions. We also note that, although the $IST1_{R51D}$ tip mutation inhibits IST1 assembly (**Fig. 6a,b**) it does not block the ability of IST1 to function in cytokinesis (**Fig. 5**), implying that there are different requirements for IST1 assembly *in vitro* and abscission function *in vivo*. Finally, in addition to tip contacts, at least one more protein-protein interface is required to create two-dimensional surfaces in helices or sheets. These secondary interaction(s) are disfavored by C-terminal autoinhibitory interactions (ref. 6 and this work) and may correspond to one of the several different kinds of higher-order packing interactions that have been proposed on the basis of cryo-EM analyses of helical ESCRT-III protein assemblies[6,7].

Our $IST1_{NTD}$ structure revealed that the downstream flap and autoinhibitory helix can fold back against the ESCRT-III core, and this topology was unambiguously established by high-quality electron density throughout the flap region (**Fig. 2** and **Supplementary Fig. 1**). Analogous models can be built for the $CHMP3_{8–183}$ and $CHMP3_{8–222}$ structures, although in those cases the connectivity has not been established unambiguously. Nevertheless, we suggest that all of these structures probably correspond to the closed, autoinhibited ESCRT-III conformation, for several reasons: (i) both $IST1_{NTD}$ and $CHMP3_{8–222}$ are monomers in solution under the conditions used for crystallization (although $IST1_{NTD}$ polymerizes under low-salt conditions) (**Fig. 1**); (ii) IST1 is redistributed into the insoluble membrane-bound, assembled fractions of cellular extracts by mutations that disrupt core packing of the autoinhibitory elements (**Supplementary Fig. 4**); (iii) CHMP3 and CHMP2A can be activated for co-assembly by deletions that remove the autoinhibitory helices from CHMP2A[6] or CHMP3, or by point mutations that destabilize packing of the CHMP3 autoinhibitory helix against the core (**Fig. 7**); (iv) mutations that remove the autoinhibitory helix or destabilize its core packing interactions render CHMP3 a dominant inhibitor of HIV-1 budding[17,20] (**Fig. 8**). Nevertheless, there is also good evidence that additional contacts beyond those visualized in our $IST1_{NTD}$ or CHMP3 structures help to stabilize the closed CHMP3 conformation even further, because point mutations in the autoinhibitory helix-core interface do not activate CHMP3 to the same extent as does deletion of the entire autoinhibitory region (**Figs. 7c** and **8**), and because short

C-terminal deletions downstream of the autoinhibitory α5 helix can also enhance ESCRT-III membrane binding and inhibition of HIV-1 budding, albeit to a lesser extent than deletions that include α5 (refs. 17,20). These observations indicate that the terminal ESCRT-III helix 6 (and possibly also flap sequences) make energetically important contacts that favor the closed ESCRT-III conformation.

In summary, many ESCRT-III proteins can adopt two distinct conformational states[6,16–21], and our studies provide a molecular model for the closed, monomeric state adopted by ESCRT-III proteins when they are distributed throughout the cytoplasm (or loosely associated with nonspecific membranes)[34]. Primary sequence and secondary-structure analyses indicate that all ESCRT-III proteins have analogous α5 helices in equivalent positions, and the mechanism of autoinhibition described here is probably quite general (**Supplementary Fig. 5a**). Surrounding elements can vary substantially in sequence, length and secondary structure, however, and they probably mediate various protein-protein interactions[33]. Notably, these different protein-protein interactions can be enhanced, inhibited or unchanged by mutations that favor the open states of various ESCRT-III proteins (for example, refs. 21,22,28,33). Thus, changes in protein-protein and protein-membrane interactions that accompany ESCRT-III activation and assembly are likely to reflect the conformational changes described here, coupled with avidity effects created by the assembly of oligomeric ESCRT-III protein arrays.

METHODS

Methods and any associated references are available in the online version of the paper at http://www.nature.com/nsmb/.

Accession Codes. Protein Data Bank: Coordinates and structure factor amplitudes have been deposited for the two $IST1_{NTD}$ crystal forms (3FRR and 3FRS), $CHMP_{8–222}$ (3FRT) and $CHMP3_{1–150}$ (3FRV).

Note: Supplementary information is available on the Nature Structural & Molecular Biology website.

ACKNOWLEDGMENTS

Portions of this research were carried out at the Stanford Synchrotron Radiation Light Source (SSRL), a national user facility operated by Stanford University on behalf of the US Department of Energy, Office of Basic Energy Sciences. The SSRL Structural Molecular Biology Program is supported by the Department of Energy, Office of Biological and Environmental Research and by the US National Institutes of Health (NIH), National Center for Research Resources, Biomedical Technology Program, and the National Institute of General Medical Sciences. We thank M. Babst for helpful discussions. This work was supported by NIH grants AI051174 (W.I.S.) and GM082545 (W.I.S. and C.P.H.).

Published online at http://www.nature.com/nsmb/
Reprints and permissions information is available online at http://npg.nature.com/reprintsandpermissions/

1. Hurley, J.H. ESCRT complexes and the biogenesis of multivesicular bodies. *Curr. Opin. Cell Biol.* **20**, 4–11 (2008).
2. Williams, R.L. & Urbe, S. The emerging shape of the ESCRT machinery. *Nat. Rev. Mol. Cell Biol.* **8**, 355–368 (2007).
3. Saksena, S., Sun, J., Chu, T. & Emr, S.D. ESCRTing proteins in the endocytic pathway. *Trends Biochem. Sci.* **32**, 561–573 (2007).
4. Piper, R.C. & Katzmann, D.J. Biogenesis and function of multivesicular bodies. *Annu. Rev. Cell Dev. Biol.* **23**, 519–547 (2007).
5. Hanson, P.I., Roth, R., Lin, Y. & Heuser, J.E. Plasma membrane deformation by circular arrays of ESCRT-III protein filaments. *J. Cell Biol.* **180**, 389–402 (2008).
6. Lata, S. *et al.* Helical structures of ESCRT-III are disassembled by VPS4. *Science* **321**, 1354–1357 (2008).
7. Ghazi-Tabatabai, S. *et al.* Structure and disassembly of filaments formed by the ESCRT-III subunit Vps24. *Structure* **16**, 1345–1356 (2008).
8. Teis, D., Saksena, S. & Emr, S.D. Ordered assembly of the ESCRT-III complex on endosomes is required to sequester cargo during MVB formation. *Dev. Cell* **15**, 578–589 (2008).
9. Saksena, S., Wahlman, J., Teis, D., Johnson, A.E. & Emr, S.D. Functional reconstitution of ESCRT-III assembly and disassembly. *Cell* **136**, 97–109 (2009).
10. Wollert, T., Wunder, C., Lippincott-Schwartz, J. & Hurley, J.H. Membrane scission by the ESCRT-III complex. *Nature* **458**, 172–177 (2009).
11. Bajorek, M. *et al.* Biochemical analyses of human IST1 and its function in cytokinesis. *Mol. Biol. Cell* **20**, 1360–1373 (2009).
12. Dimaano, C., Jones, C.B., Hanono, A., Curtiss, M. & Babst, M. Ist1 regulates vps4 localization and assembly. *Mol. Biol. Cell* **19**, 465–474 (2008).
13. Rue, S.M., Mattei, S., Saksena, S. & Emr, S.D. Novel Ist1–Did2 complex functions at a late step in multivesicular body sorting. *Mol. Biol. Cell* **19**, 475–484 (2008).
14. Agromayor, M. *et al.* Essential role of hIST1 in cytokinesis. *Mol. Biol. Cell* **20**, 1374–1387 (2009).
15. Babst, M., Katzmann, D., Estepa-Sabal, E., Meerloo, T. & Emr, S. Escrt-III. An endosome-associated heterooligomeric protein complex required for mvb sorting. *Dev. Cell* **3**, 271–282 (2002).
16. Muzioł, T. *et al.* Structural basis for budding by the ESCRT-III factor CHMP3. *Dev. Cell* **10**, 821–830 (2006).
17. Shim, S., Kimpler, L.A. & Hanson, P.I. Structure/function analysis of four core ESCRT-III proteins reveals common regulatory role for extreme C-terminal domain. *Traffic* **8**, 1068–1079 (2007).
18. Lata, S. *et al.* Structural basis for autoinhibition of ESCRT-III CHMP3. *J. Mol. Biol.* **378**, 818–827 (2008).
19. Lin, Y., Kimpler, L.A., Naismith, T.V., Lauer, J.M. & Hanson, P.I. Interaction of the mammalian endosomal sorting complex required for transport (ESCRT) III protein hSnf7–1 with itself, membranes, and the AAA+ ATPase SKD1. *J. Biol. Chem.* **280**, 12799–12809 (2005).
20. Zamborlini, A. *et al.* Release of autoinhibition converts ESCRT-III components into potent inhibitors of HIV-1 budding. *Proc. Natl. Acad. Sci. USA* **103**, 19140–19145 (2006).
21. Kieffer, C. *et al.* Two distinct modes of ESCRT-III recognition are required for VPS4 functions in lysosomal protein targeting and HIV-1 budding. *Dev. Cell* **15**, 62–73 (2008).
22. McCullough, J., Fisher, R.D., Whitby, F.G., Sundquist, W.I. & Hill, C.P. ALIX-CHMP4 interactions in the human ESCRT pathway. *Proc. Natl. Acad. Sci. USA* **105**, 7687–7691 (2008).
23. Tsang, H.T. *et al.* A systematic analysis of human CHMP protein interactions: Additional MIT domain-containing proteins bind to multiple components of the human ESCRT III complex. *Genomics* **88**, 333–346 (2006).
24. Row, P.E. *et al.* The MIT domain of UBPY constitutes a CHMP binding and endosomal localization signal required for efficient epidermal growth factor receptor degradation. *J. Biol. Chem.* **282**, 30929–30937 (2007).
25. Rodriguez-Galan, O., Galindo, A., Hervas-Aguilar, A., Arst, H.N. & Penalva, M.A. Physiological involvement in pH signalling of Vps24-mediated recruitment of Aspergillus PalB cysteine protease to ESCRT-III. *J. Biol. Chem.* **284**, 4404–4412 (2008).
26. Yorikawa, C. *et al.* Human calpain 7/PalBH associates with a subset of ESCRT-III-related proteins in its N-terminal region and partly localizes to endocytic membrane compartments. *J. Biochem.* **143**, 731–745 (2008).
27. Yang, D. *et al.* Structural basis for midbody targeting of spastin by the ESCRT-III protein CHMP1B. *Nat. Struct. Mol. Biol.* **15**, 1278–1286 (2008).
28. Stuchell-Brereton, M.D. *et al.* ESCRT-III recognition by VPS4 ATPases. *Nature* **449**, 740–744 (2007).
29. Obita, T. *et al.* Structural basis for selective recognition of ESCRT-III by the AAA ATPase Vps4. *Nature* **449**, 735–739 (2007).
30. Samson, R.Y., Obita, T., Freund, S.M., Williams, R.L. & Bell, S.D. A role for the ESCRT system in cell division in archaea. *Science* **322**, 1710–1713 (2008).
31. Azmi, I.F. *et al.* ESCRT-III family members stimulate Vps4 ATPase activity directly or via Vta1. *Dev. Cell* **14**, 50–61 (2008).
32. Xiao, J. *et al.* Structural basis of Vta1 function in the multivesicular body sorting pathway. *Dev. Cell* **14**, 37–49 (2008).
33. Shim, S., Merrill, S.A. & Hanson, P.I. Novel interactions of ESCRT-III with LIP5 and VPS4 and their implications for ESCRT-III disassembly. *Mol. Biol. Cell* **19**, 2661–2672 (2008).
34. Welsch, S. *et al.* Ultrastructural analysis of ESCRT proteins suggests a role for endosome-associated tubular-vesicular membranes in ESCRT function. *Traffic* **7**, 1551–1566 (2006).
35. Baker, N.A., Sept, D., Joseph, S., Holst, M.J. & McCammon, J.A. Electrostatics of nanosystems: application to microtubules and the ribosome. *Proc. Natl. Acad. Sci. USA* **98**, 10037–10041 (2001).

ONLINE METHODS

Expression vectors and antibodies. Vectors and antibodies are summarized in **Supplementary Tables 1** and **2**.

Protein expression and purification. We expressed IST1 and CHMP proteins in *Escherichia coli* with N-terminal GST-affinity tags. Protein expression, purification and tag removal are described in the **Supplementary Methods**.

Equilibrium sedimentation analyses. We centrifuged purified CHMP3, $CHMP3_{8–222}$ and $IST1_{NTD}$ in 10 mM Tris-HCl pH 8.0, 100 mM NaCl (CHMP3 proteins) or 50 mM Tris-HCl pH 7.0, 350 mM NaCl and 1 mM DTT ($IST1_{NTD}$) at 4 °C in an Optima XL-A centrifuge (Beckman). Initial protein concentrations are given in **Figure 1a–c**. Data were collected after equilibrium was reached at two speeds (20,000 r.p.m. and 24,000 r.p.m.) in a Beckman An-60 Ti rotor, and the molecular masses were determined from the resulting six data sets for each protein by globally fitting to single ideal species models using the nonlinear least-squares algorithms in the Heteroanalysis software[36]. Protein partial specific volumes and solvent densities were calculated with the program SEDNTERP (version 1.09)[37].

Protein crystallization and data collection. We crystallized $IST1_{NTD}$, $CHMP3_{8–222}$ and $CHMP3_{1–150}$ by vapor diffusion at 13 °C. $IST1_{NTD}$ crystals grew from a 12 mg ml^{-1} solution in gel filtration buffer. Crystal form I (diamond-shaped morphology, $P4_32_12$, 1 molecule per asymmetric unit) grew in 1–3 d by simple dehydration of a 2-µl drop. Crystals were cryoprotected by passage through silica oil, suspended in a nylon loop and plunged into liquid nitrogen. Crystal form II (rods and plates, $P2_1$, 1 molecule per asymmetric unit) grew from a 1:1 (v/v) mixture of protein and well solution (180 mM KCl, 50 mM HEPES pH 7.6, 35% pentaethritol propexylate and 7% (v/v) ethylene glycol). Crystals were cryo-cooled directly without solution modification. Native data for both crystal forms were collected on a Rigaku Micromax 007HF rotating anode generator equipped with VeriMax-HR optics.

$CHMP3_{8–222}$ crystals (flat plates, $P2_1$, 2 molecules per asymmetric unit) grew from a 1:2 (v/v) mixture of protein (30 mg ml^{-1} in gel filtration buffer) and well solution (10–22% PEG 6000 and 0.1M Na-HEPES pH 7.0–8.0). Data were collected at SSRL beamline 11-1. $CHMP3_{1–150}$ crystals (hexagonal rods, $P6_1$) grew from a 1:1 (v/v) mixture of protein (22 mg ml^{-1} in gel filtration buffer) and well solution (16% (v/v) PEG 3350, 0.1 M Na HEPES pH 7.0–8.0, 200 mM proline). Data were collected on a rotating anode generator. Despite extensive effort, we were unable to collect better data at the synchrotron. Data were indexed and scaled with the program HKL2000 (ref. 38) (**Table 1**).

Structure determinations. We collected three-wavelength MAD data from selenomethionine-substituted $IST1_{NTD}$ at SSRL beamline 9–1 to 3.4 Å. Three of the six potential selenium sites were identified using SOLVE[39], and the resulting 4.0-Å phases were solvent flattened and extended to 2.6-Å resolution using the native data and the program DM[40]. The four core helices (α1–α4) were built using O[41], and this partial model was used for molecular replacement determination of the higher-resolution form II crystal structure using PHASER[42]. The models were completed with COOT[43], refined with REFMAC5 (ref. 44) and analyzed using programs within the CCP4 suite[45]. The similar $IST1_{NTD}$ structures in the two crystal forms overlapped with an r.m.s. deviation of 1.25 Å on Cα atoms 12–170.

We determined both CHMP3 structures by molecular replacement using the published $CHMP3_{8–183}$ structure (PDB 2GD5)[16] as the search model. The correctness of the solutions is supported by PHASER[42] Z-scores of 9.1 ($CHMP3_{8–222}$) and 8.6 ($CHMP3_{1–150}$) and by the appearance of electron density when portions of the search model were omitted from the molecular replacement calculation (**Supplementary Fig. 2**). Both structures are hampered by low resolution and a correspondingly low number of unique reflections. R_{free} sets of 5% contain too few reflections (~120) to be statistically useful. An optimal strategy was therefore determined by considering R_{free} values from multiple refinement runs, each starting from the same molecular replacement solution and with a different small number (~200) of reflections in the test set. This indicated that the best results were obtained using rigid-body refinement in PHENIX[46] with each helix treated as a rigid unit. This approach was therefore applied to the starting molecular replacement solution but using all of the reflections in the calculation (no test set).

Biosensor binding assays. We used BIACORE2000 and BIACORE3000 instruments (GE Healthcare) to measure the binding of pure recombinant CHMP1B to immobilized GST-$IST1_{NTD}$ proteins captured from *E. coli* extracts[28], as described in **Supplementary Methods**.

IST1 depletion and rescue experiments. We transfected HeLa-M cells with IST1 expression vectors (1 µg per well, using Lipofectamine 2000, Invitrogen) and siRNA (20nM, Lipofectamin RNAi MAX, Invitrogen) following the time course: $t = 0$, seed cells in DMEM and 10% (v/v) FCS (six-well plates, 4×10^5 cells per well); $t = 24$ h, add IST1 expression vector; $t = 32$ h, change media and add IST1 vector; $t = 44$ h, trypsinize and reseed cells on 18-mm glass cover slips for immunofluorescence analyses (3×10^4 cells per cover slip) and in six-well plates for western blotting (3×10^5 cells per well); $t = 56$ h, change media and add siRNA; $t = 68$ h, change media and add siRNA; $t = 94$ h, fix or harvest cells and analyze.

Direct visualization of cytokinesis defects. We fixed transfected HeLa-M cells with 4% (v/v) paraformaldehyde and stained with SYTOX Green (Invitrogen) and with mouse anti–α-tubulin and a secondary Alexa 594–conjugated goat anti-mouse antibody. We scored midbody arrest manually for ≥3 blinded sets of 200 cells by direct visualization using fluorescence microscopy.

ESCRT-III assembly reactions. Assembly conditions for CHMP2A and CHMP3, $IST1_{NTD}$, and CHMP1B proteins are provided in the **Supplementary Methods**.

Transmission electron microscopy. We analyzed assembly reactions using TEM with negative staining. Carbon-coated grids were placed on aliquots of each assembly reaction (7 µl, 90 s), washed with 3–4 drops of 0.1 M KCl, stained with 3–4 drops of 4% (v/v) uranyl acetate, air dried and imaged (Hitachi 7100 TEM).

GST pull-down assays. We tested the binding of pure recombinant CHMP2A proteins to various GST-CHMP3 proteins as described in the **Supplementary Methods**.

HIV-1 vector release and infectivity. We co-transfected 293T cells with vectors expressing CHMP3-Myc and HIV-1 and harvested supernatants and cells after 24 h. Western blotting was used to analyze cellular proteins and virions pelleted through 20% sucrose cushion and HeLa-M cell transduction to measure vector titers. Full details are provided in **Supplementary Methods**.

36. Cole, J.L. Analysis of heterogeneous interactions. *Methods Enzymol.* **384**, 212–232 (2004).
37. Laue, T., Shah, B., Ridgeway, T. & Pelletier, S. Computer-aided interpretation of analytical sedimentation data for proteins. in *Ultracentrifugation in Biochemistry and Polymer Science* (eds. Rowe, A. & Horton, J.) 90–125 (Royal Society of Chemistry, Cambridge, UK, 1992).
38. Otwinowski, Z. Oscillation data reduction program. in *Data Collection and Processing* (eds. Sawyer, L., Isaacs, N. & Bailey, S.) 56–62 (SERC Daresbury Laboratory, Warrington, UK, 1993).
39. Terwilliger, T.C. & Berendzen, J. Automated structure solution for MIR and MAD. *Acta Crystallogr. D Biol. Crystallogr.* **55**, 849–861 (1999).
40. Cowtan, K.D. & Zhang, K.Y. Density modification for macromolecular phase improvement. *Prog. Biophys. Mol. Biol.* **72**, 245–270 (1999).
41. Jones, T.A., Zou, J.Y., Cowan, S.W. & Kjeldgaard, M. Improved methods for binding protein models in electron density maps and the location of errors in these models. *Acta Crystallogr. A* **47**, 110–119 (1991).
42. McCoy, A.J., Grosse-Kunstleve, R.W., Storoni, L.C. & Read, R.J. Likelihood-enhanced fast translation functions. *Acta Crystallogr. D Biol. Crystallogr.* **61**, 458–464 (2005).
43. Emsley, P. & Cowtan, K. Coot: model-building tools for molecular graphics. *Acta Crystallogr. D Biol. Crystallogr.* **60**, 2126–2132 (2004).
44. Murshudov, G.N., Vagin, A.A. & Dodson, E.J. Refinement of macromolecular structures by the maximum-likelihood method. *Acta Crystallogr. D Biol. Crystallogr.* **53**, 240–255 (1997).
45. Collaborative Computational Project, Number 4. The CCP4 suite: programs for protein crystallography. *Acta Crystallogr D* **50**, 760–763 (November 4, 1994).
46. Zwart, P.H. *et al.* Automated structure solution with the PHENIX suite. *Methods Mol. Biol.* **426**, 419–435 (2008).

SUPPLEMENTARY MATERIAL

Structural Basis for ESCRT-III Protein Autoinhibition

Monika Bajorek[1], Heidi L. Schubert[1], John McCullough[1], Charles Langelier, Debra M. Eckert, William-May B. Stubblefield, Nathan T. Uter, David G. Myszka, Christopher P. Hill*, Wesley I. Sundquist*

Nature Structural & Molecular Biology: doi:10.1038/nsmb.1621

Supplementary Figures

a

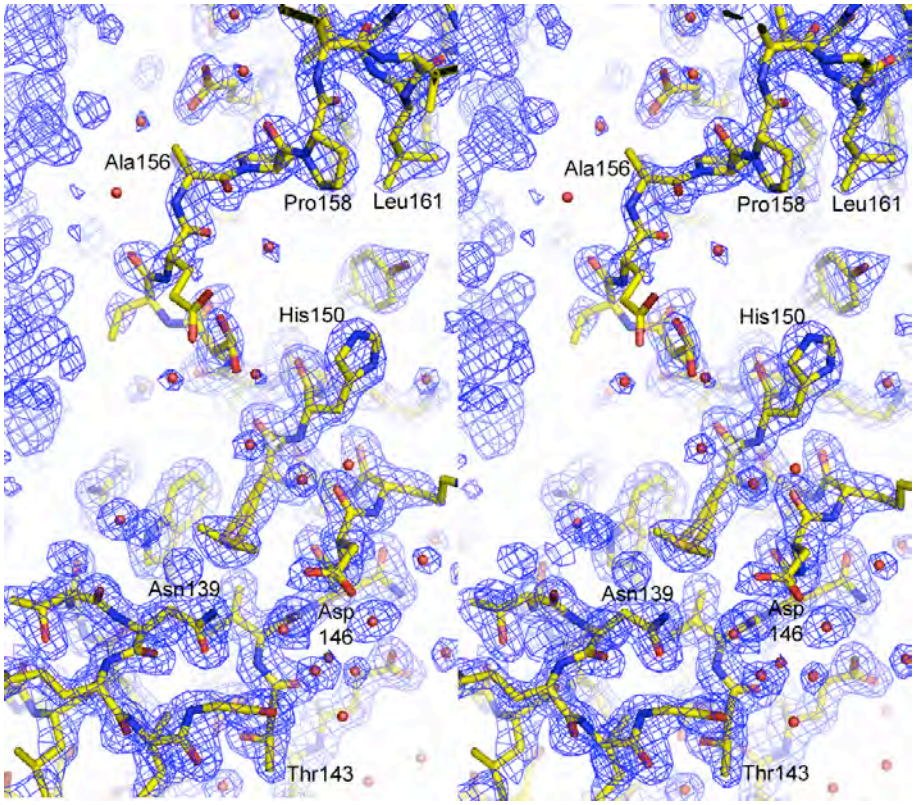

b

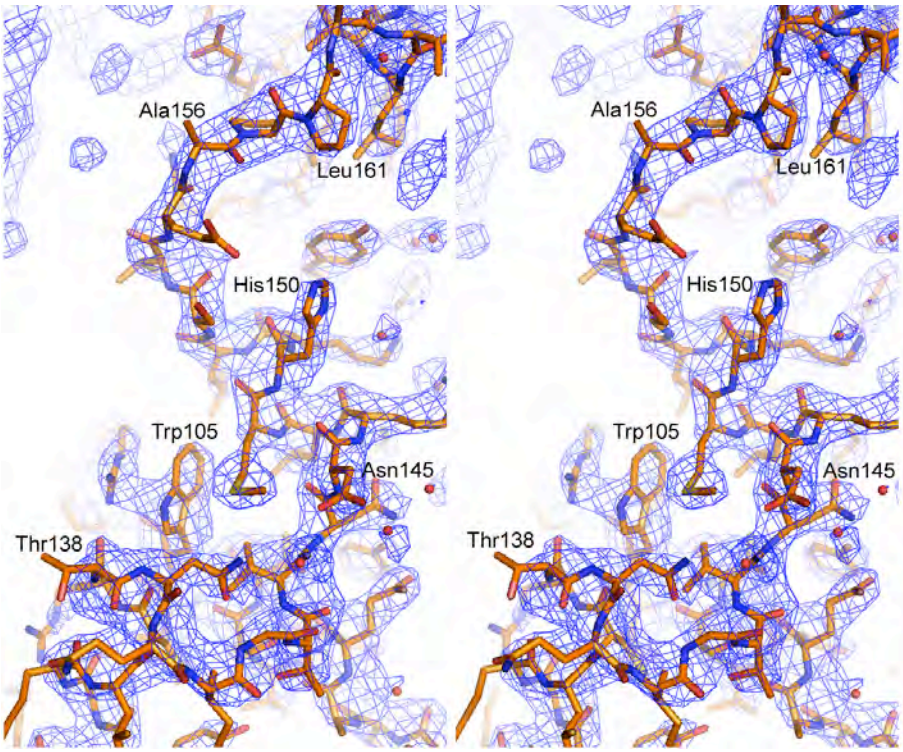

Supplementary Figure 1 Representative electron density (2Fo-Fc, 1σ x RMSD) surrounding the flap region in the $IST1_{NTD}$ crystal structures.
(a) $P2_1$ crystal form (1.8Å resolution).
(b) $P4_32_12$ crystal form (2.6Å resolution).

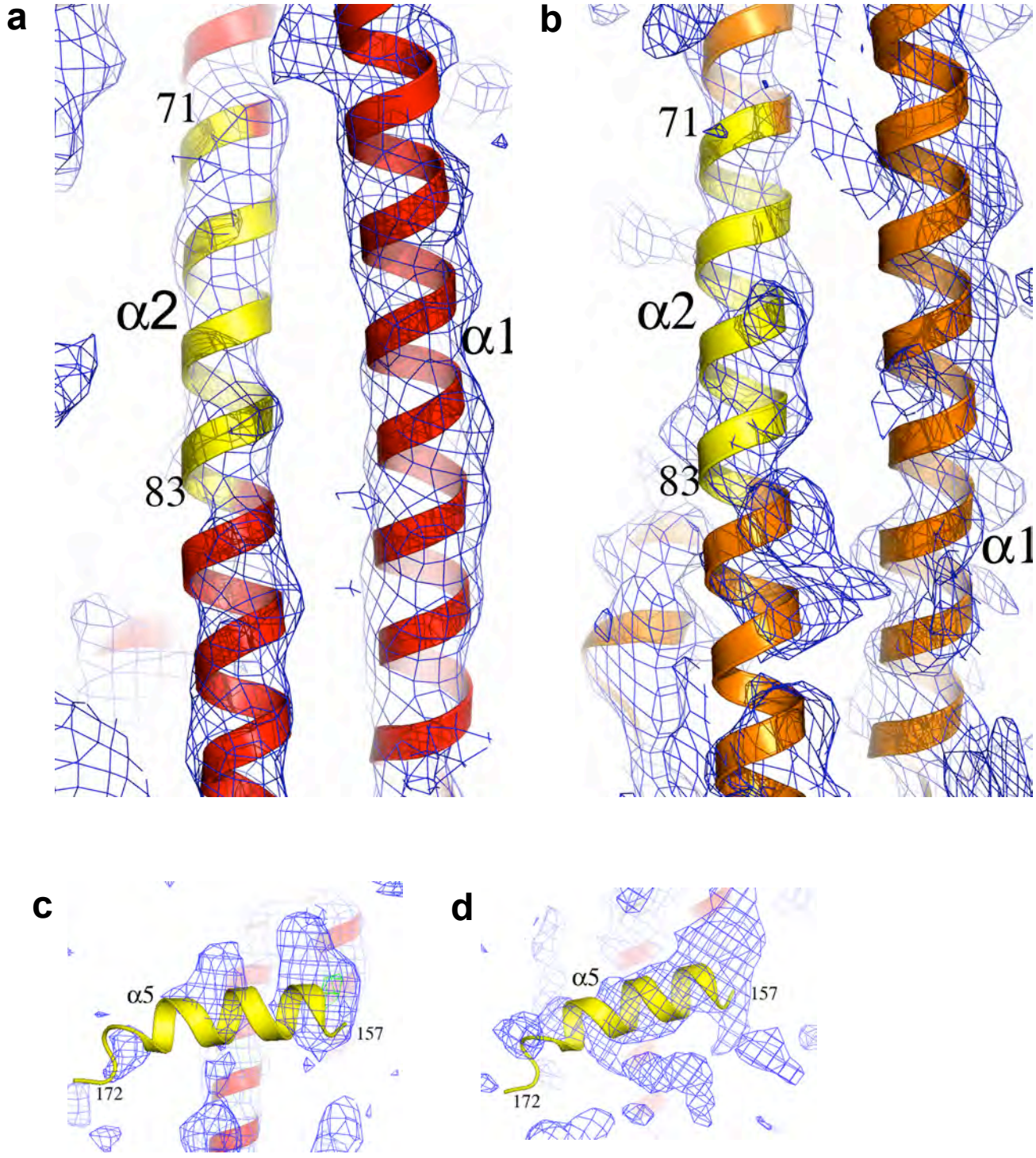

Supplementary Figure 2 Representative and unbiased electron density (2Fo-Fc, 1σ x RMSD) for the CHMP3 crystal structures. Regions in yellow were omitted from the model prior to molecular replacement.
(a) $CHMP3_{8-222}$ α1 and α2 region (residues 71-83 omitted) (4.0 Å resolution).
(b) $CHMP3_{1-150}$ α1 and α2 region (residues 71-83 omitted) (3.7Å resolution).
(c,d) Unbiased density for the autoinhibitory helix in both molecules of the $CHMP3_{8-222}$ asymmetric unit.

a ($IST1_{NTD}$-$P2_1$)

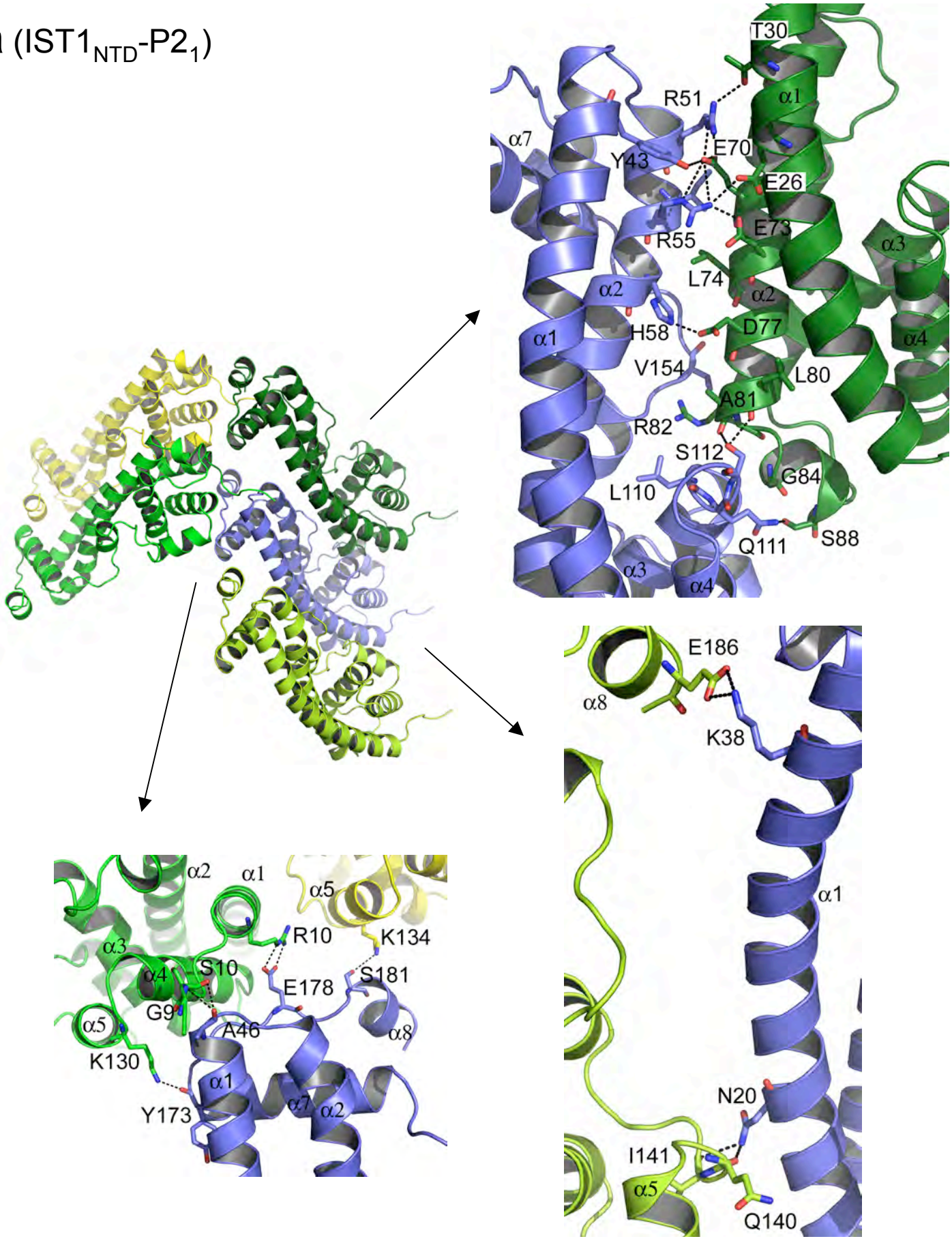

b ($IST1_{NTD}$, $P4_32_12$)

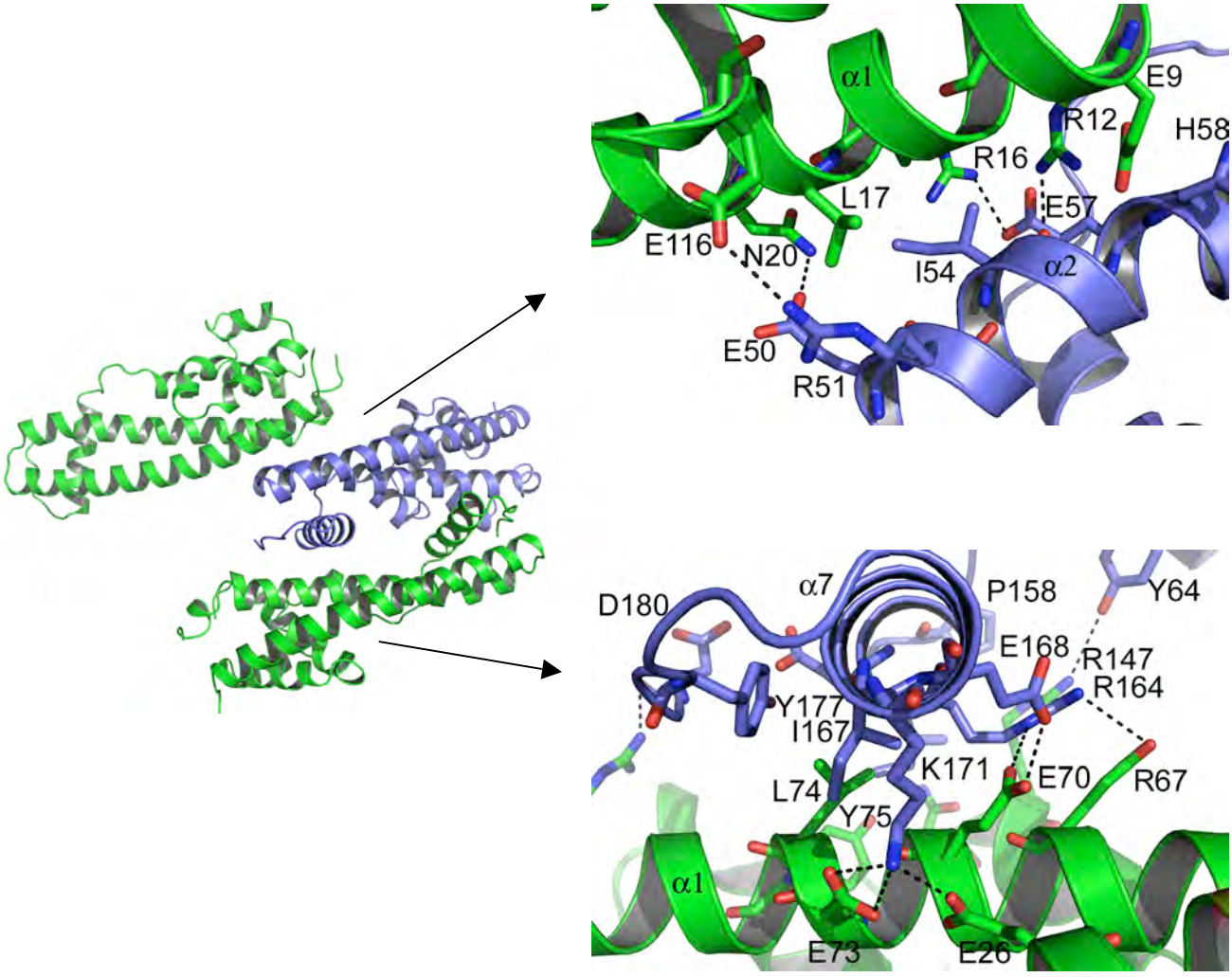

Nature Structural & Molecular Biology: doi:10.1038/nsmb.1621

c ($CHMP3_{8-222}$)

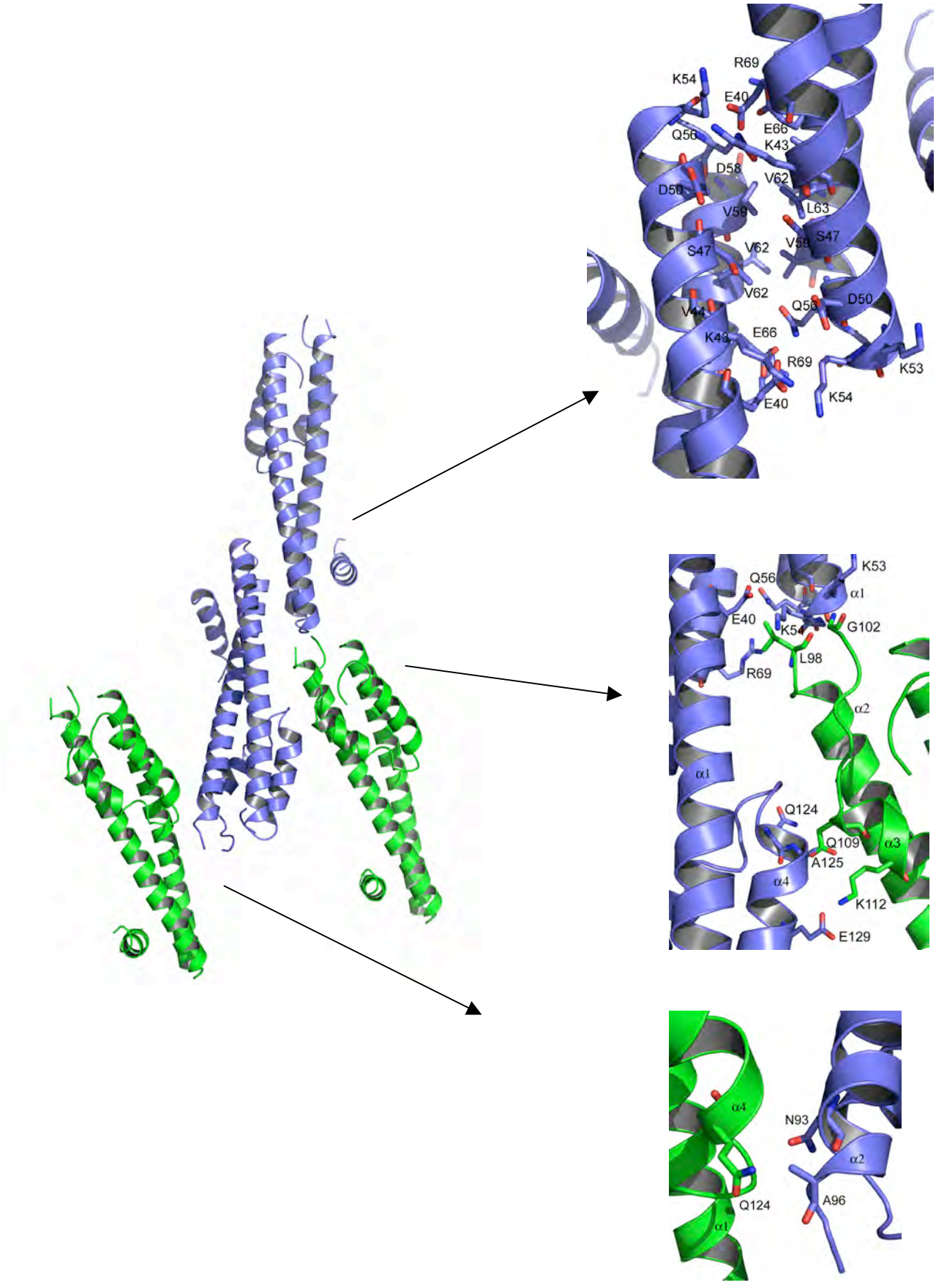
R69
K54
E40
Q56
E66
K43
D58
V62
D50
L63
V59
S47
V62
V59
S47
V62
V62
Q56
D50
V44
E66
K43
R69
K53
E40
K54
K53
Q56
α1
E40
K54
G102
L98
R69
α2
α1
Q124
Q109
α3
A125
α4
K112
E129
α4
N93
α2
Q124
A96
α1

d ($CHMP3_{1-150}$)

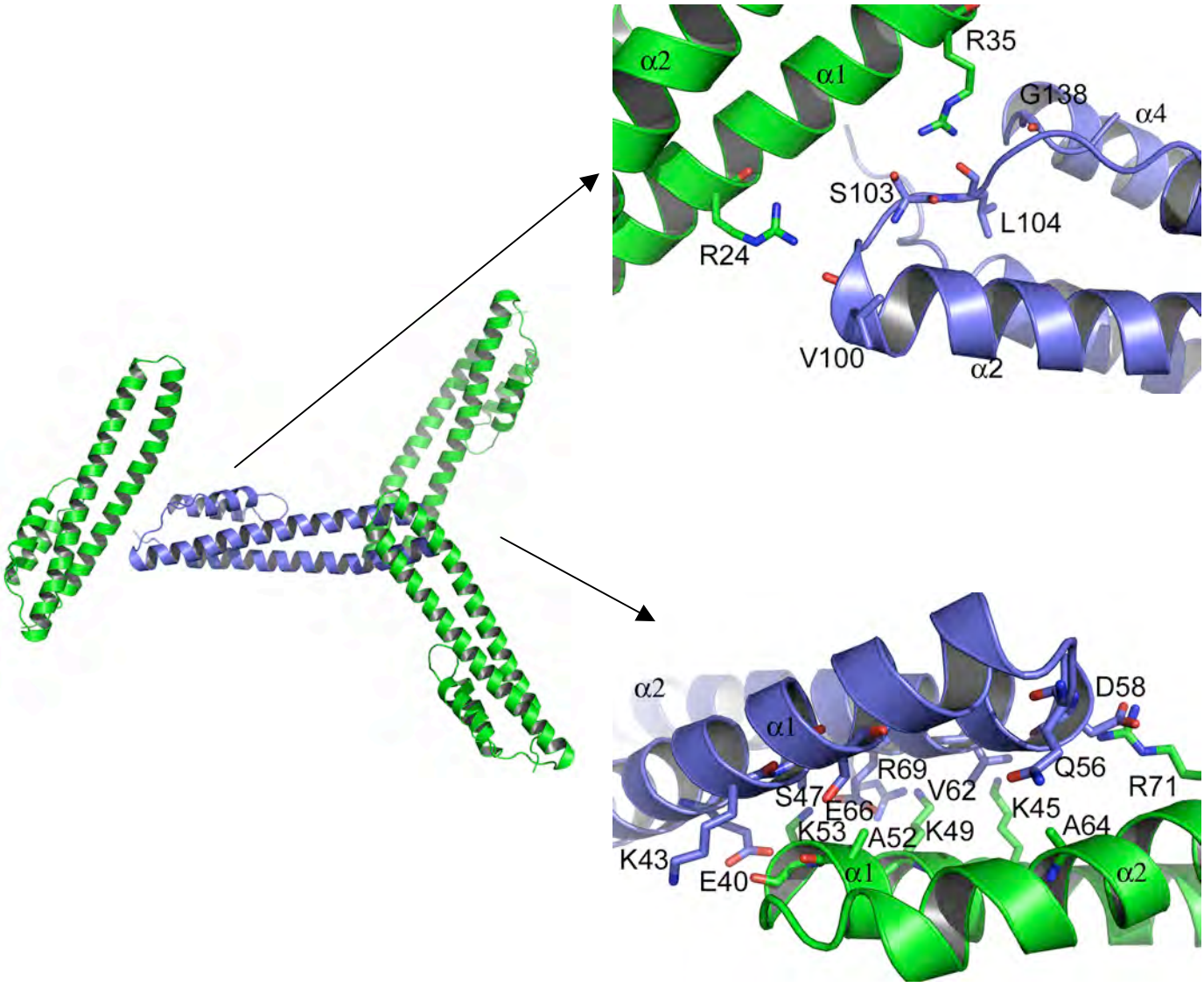

Supplementary Figure 3 Lattice contacts in different $IST1_{NTD}$ and CHMP3 crystal forms. Contacts shown were identified using the CCP4 program CONTACT[1].
(a) Overview and detailed views of $IST1_{NTD}$ $P2_1$ crystal contacts.
(b) Overview and detailed views of $IST1_{NTD}$ $P4_32_12$ crystal contacts.
(c) Overview and detailed views of $CHMP3_{8-222}$ crystal contacts.
(d) Overview and detailed views of $CHMP3_{1-150}$ crystal contacts.

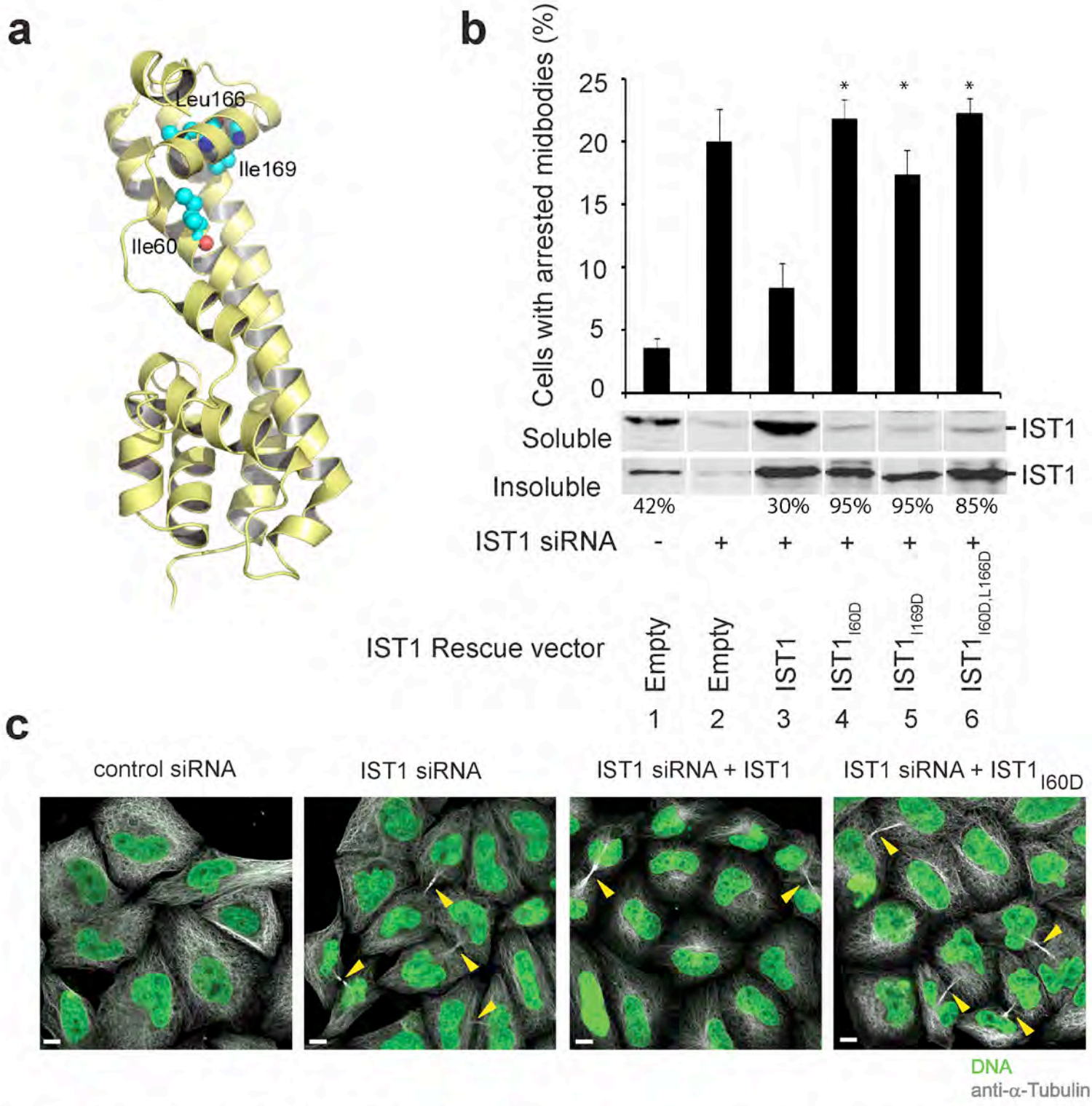

Supplementary Figure 4 IST1 activation in vivo.
(a) Ribbon diagram showing the location of the mutated IST1 Ile60, Leu166 and Ile169 residues within the interface between a2 and the autoinhibitory helix a5.
(b) Quantification of the cytokinesis defects from panel **c** (below), and western blots showing partitioning of wild type and mutant IST1 proteins between the soluble state (upper blot) and the insoluble membrane-bound/assembled state (lower blot). Quantified percentages of insoluble proteins are shown below the blot.
(**c**) Immunofluorescence images showing the midbody phenotypes of cells following designated siRNA treatments and re-expression of wild type IST1 or IST1I60D (final two panels). Microtubules (anti-a-Tubulin, grey) and nuclei (SYTOX green) were stained for reference, and yellow arrowheads highlight midbodies. Scale bars are 10 μm.

Nature Structural & Molecular Biology: doi:10.1038/nsmb.1621

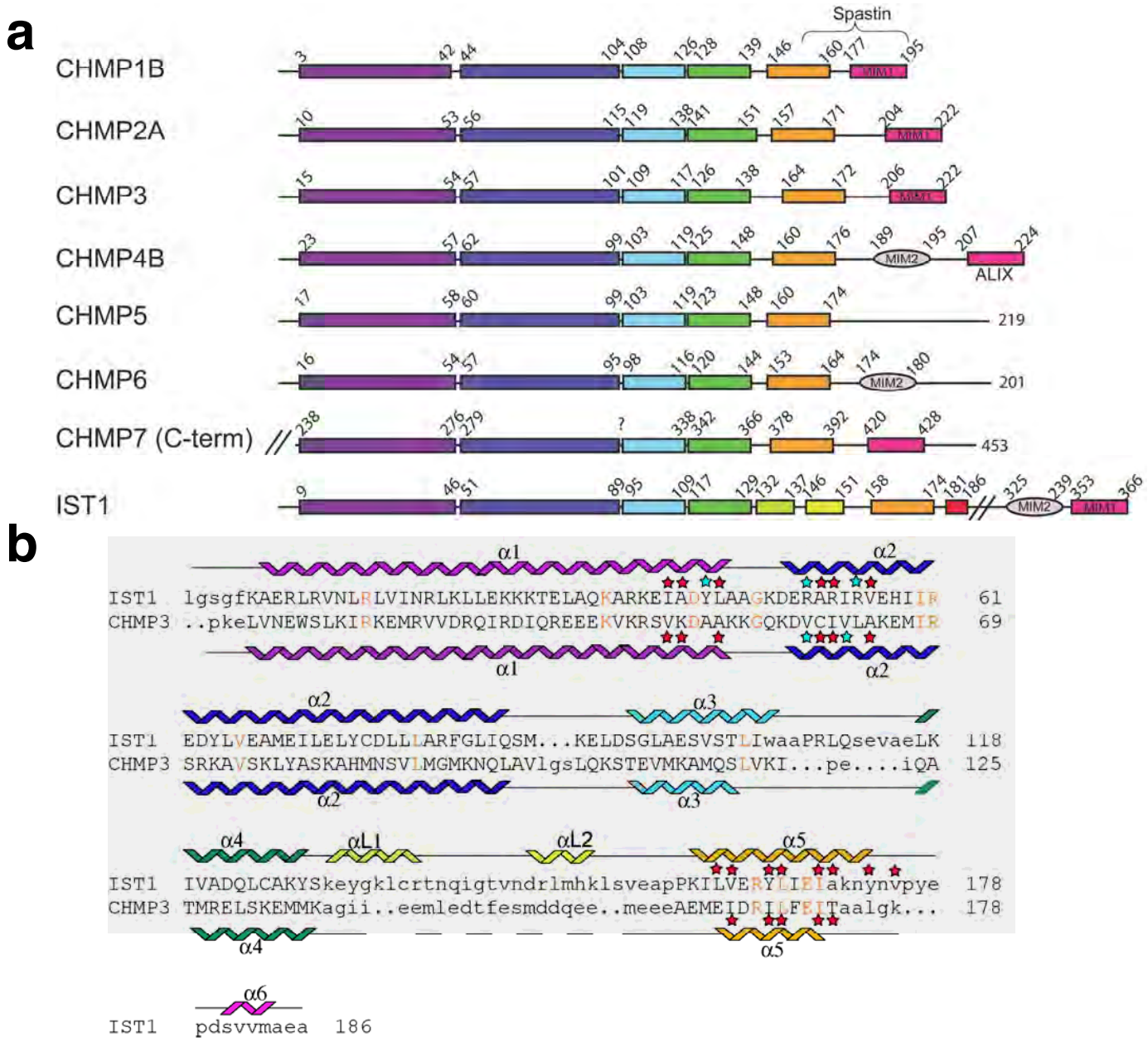

Supplementary Figure 5 Secondary structural models and alignments of human ESCRT-III proteins.

(a) Secondary structural models of human ESCRT-III proteins. The figure shows known (CHMP3 and $IST1_{NTD}$) or predicted secondary structures of representative members from the eight different families of human ESCRT-III proteins. Helices are shown as blocks, and colors match the scheme of Fig. 2a-c. ESCRT-III core domain helices (α1-α4) are colored purple-green, and autoinhibitory helices are shown in orange. Approximate residue boundaries for each helix are provided above each secondary structure. Downstream elements show predicted helices (boxes), the two known classes of VPS4 MIT domain interacting motifs (MIM1, magenta and MIM2, pink), the binding site for the Spastin MIT domain on CHMP1B, and the binding site for the ALIX Bro1 domain on CHMP4B. Note that the C-terminal core domain of CHMP7 was used in the illustration and that, in several cases, α2-α4 segments were predicted as continuous helices and were manually separated into α2, α3, and α4 helices.

(b) Structure-based sequence alignment between the N-terminal domains of $IST1_{NTD}$ and CHMP3. Uppercase residues were included in the alignment (126 residues aligned, RMSD=3.0Å). Red residues are conserved between the two proteins (8% overall sequence identity). Secondary structures are depicted above and below their corresponding sequences, with color coding that matches Fig. 2 and Supplementary Fig. 5a. Red stars denote resides within the α5-α1/α2 interface and cyan stars denote tip-to-tip mutants that inhibit polymerization *in vitro*.

Supplementary Table 1. Protein Expression Vectors

a. Bacterial Expression Vectors

Plasmid Name	Source[(a)]	Internal ID	Generation	Epitope Tags
pGEX	Amersham	WISP 01-69		N-term GST
pGEX.CHMP3	NP_057163	WISP 02-94	NdeI/BamHI cloning	N-term GST
pGEX.CHMP3.8-222	NP_057163	WISP 07-213	Quikchange Mutagenesis	N-term GST
pGEX.CHMP3.1-150	NP_057163	WISP 08-214	Quikchange Mutagenesis	N-term GST
pGEXCHMP3.I168D.L159D	NP_057163	WISP 08-215	Quikchange Mutagenesis	N-term GST
pGEX.CHMP3.V48D.A64D	NP_057163	WISP 08-216	Quikchange Mutagenesis	N-term GST
pGEX.CHMP3.V59D.V62D	NP_057163	WISP 09-26	Quikchange Mutagenesis	N-term GST
pGEX.CHMP3.V59D.V62D.I168D.L169D	NP_057163	WISP 09-29	Quikchange Mutagenesis	N-term GST
pGEX.CHMP2A	NP_055268	WISP 02-82	NdeI/BamHI cloning	N-term GST
pGEX.IST1.1-189	BC103745	WISP 07-74	NdeI/BamHI cloning	N-term GST
pGEX.IST1.1-189.R51D	BC103745	WISP 08-220	Quikchange Mutagenesis	N-term GST
pGEX.IST1.1-189.E39A	BC103745	WISO 09-38	Quikchange Mutagenesis	N-term GST
pGEX.IST1.1-189.Y43D	BC103745	WISP 09-39	Quikchange Mutagenesis	N-term GST
pGEX.IST1.1-189.K48D	BC103745	WISP 09-40	Quikchange Mutagenesis	N-term GST
pGEX.IST1.1-189.I54D	BC103745	WISP 09-41	Quikchange Mutagenesis	N-term GST
pGEX.IST1.1-189.R55D	BC103745	WISP 09-42	Quikchange Mutagenesis	N-term GST
pGEX.IST1.1-189.E67A	BC103745	WISP 09-43	Quikchange Mutagenesis	N-term GST
pGEX.IST1.1-189.E70A	BC103745	WISP 09-44	Quikchange Mutagenesis	N-term GST
pGEX.IST1.1-189.L74R	BC103745	WISP 09-45	Quikchange Mutagenesis	N-term GST
pGEX.IST1.1-189.Y75R	BC103745	WISP 09-46	Quikchange Mutagenesis	N-term GST
pGEX.IST1.1-189.L78R	BC103745	WISP 09-47	Quikchange Mutagenesis	N-term GST
pGEX.IST1.1-189.V56D	BC103745	WISP 09-48	Quikchange Mutagenesis	N-term GST
pGEX.IST1.1-189.I60D	BC103745	WISP 09-49	Quikchange Mutagenesis	N-term GST
pGEX.IST1.1-189.L166D	BC103745	WISP 09-50	Quikchange Mutagenesis	N-term GST
pGEX.IST1.1-189.I169D	BC103745	WISP 09-51	Quikchange Mutagenesis	N-term GST
pGEX.IST1.1-189.D63A	BC103745	WISP 09-52	Quikchange Mutagenesis	N-term GST
pGEX.IST1.1-189.Y64A	BC103745	WISP 09-53	Quikchange Mutagenesis	N-term GST
pGEX.IST1.1-189.R164D	BC103745	WISP 09-54	Quikchange Mutagenesis	N-term GST
pGEX.IST1.1-189.Y165A	BC103745	WISP 09-55	Quikchange Mutagenesis	N-term GST
pGEX.IST1.1-189.E168R	BC103745	WISP 09-56	Quikchange Mutagenesis	N-term GST
pGEX.CHMP1B	AAG01449	WISP 08-221	NdeI/BamHI cloning	N-term GST

Nature Structural & Molecular Biology: doi:10.1038/nsmb.1621

b. Mammalian Expression Vectors

Plasmid Name	Source[(a)]	Internal ID	Generation	Epitope Tags
pcDNA3.1/myc-His(-)A	Invitrogen	WISP 02-257		C-term Myc
pCAG.MCS2.C-Myc	Internal	WISP 08-104		C-term Myc
pCAG.Myc	(b)	WISP 06-64		N-term Myc
pCAG.OSF	Modified from pCAG.Myc	WISP 06-65		N-term Myc
pcDNA IST1.siRNA1res	BC103745	WISP 08-33	XhoI/BamHI cloning	None
pcDNA IST1.I60D.siRNA1res	BC103745	WISP 08-217	Quikchange Mutagenesis	None
pcDNA IST1.R51D.siRNA1res	BC103745	WISP 09-30	Quikchange Mutagenesis	None
pcDNA IST1.E67A.siRNA1res	BC103745	WISP 09-31	Quikchange Mutagenesis	None
pcDNA IST1.D63A.siRNA1res	BC103745	WISP 09-32	Quikchange Mutagenesis	None
pcDNA IST1.Y64A.siRNA1res	BC103745	WISP 09-33	Quikchange Mutagenesis	None
pcDNA IST1.Y165A.siRNA1res	BC103745	WISP 09-34	Quikchange Mutagenesis	None
pcDNA IST1.E168R.siRNA1res	BC103745	WISP 09-35	Quikchange Mutagenesis	None
pcDNA IST1.L166D.siRNA1res	BC103745	WISP 08-218	Quikchange Mutagenesis	None
pcDNA IST1.I169D.siRNA1res	BC103745	WISP 09-36	Quikchange Mutagenesis	None
pcDNA IST1.I60D.L166D.siRNA1res	BC103745	WISP 09-37	Quikchange Mutagenesis	None
pCAG.CHMP3.Myc	NP_057163	WISP 08-99	XhoI/KpnI cloning	C-term Myc
pCAG.CHMP3.1-150.Myc	NP_057163	WISP 08-208	Xho1/Kpn1 cloning	C-term Myc
pCAG.CHMP3.I168D.L169D.Myc	NP_057163	WISP 08-209	Xho1/Kpn1 cloning	C-term Myc
pCAG.CHMP3.V48D.I168D.L169D.Myc	NP_057163	WISP 09-235	XhoI/KpnI cloning	C-term Myc
pCAG.OSF.IST1.1-189	BC103745	WISP 08-28	KpnI/XhoI cloning	N-term OSF
pCAG.OSF.IST1.1-189.E39A	BC103745	WISP 09-1	KpnI/XhoI cloning	N-term OSF
pCAG.OSF.IST1.1-189.R51D	BC103745	WISP 09-2	KpnI/XhoI cloning	N-term OSF
pCAG.OSF.IST1.1-189.R55D	BC103745	WISP 09-4	KpnI/XhoI cloning	N-term OSF
pCAG.OSF.IST1.1-189.I60D	BC103745	WISP 09-6	KpnI/XhoI cloning	N-term OSF
pCAG.OSF.IST1.1-189.E67A	BC103745	WISP 09-7	KpnI/XhoI cloning	N-term OSF
pCAG.OSF.IST1.1-189.E70A	BC103745	WISO 09-8	KpnI/XhoI cloning	N-term OSF
pCAG.OSF.IST1.1-189.I74R	BC103745	WISP 09-9	KpnI/XhoI cloning	N-term OSF
pCAG.OSF.IST1.1-189.Y75A	BC103745	WISP 09-10	KpnI/XhoI cloning	N-term OSF
pCAG.OSF.IST1.1-189.L78R	BC103745	WISP 09-11	KpnI/XhoI cloning	N-term OSF
pCAG.Myc.CHMP1A	AF281063	WISP 08-77	XhoI/KpnI cloning	N-term Myc

a. Except for commercial vectors, "Source" corresponds to the source of the inserted gene. For IST1 and CHMP1 constructs, this corresponds to the NCBI gene accession number. For all other constructs these correspond to NCBI protein accession numbers.

b. Madaule P, Eda M, Watanabe N, Fujisawa K, Matsuoka T, Bito H, Ishizaki T, Narumiya S.(1998) Role of citron kinase as a target of the small GTPase Rho in cytokinesis. Nature. 394:491-494.

Nature Structural & Molecular Biology: doi:10.1038/nsmb.1621

Supplementary Table 2. Antibodies

Name	Host	Clone#	Working Dilution	Conjugation	Experiment	Source
Myc	Mouse	9E10	1:3,000	none	WB	Covance
HIV-CA	Rabbit	polyclonal	1:5,000	none	WB	Covance
α-Tubulin	Mouse	DM1A	1:5,000	none	WB	Sigma
α-Tubulin	Mouse	DM1A	1:1,000	none	ICC	Sigma
IST1	Rabbit	polyclonal	1:5,000	none	WB	Covance
CHMP2A	Rabbit	polyclonal	1:200	none	WB	Covance
GST	Rabbit	polyclonal	1:1,000	none	WB	Upstate
mouse IgG	Goat	polyclonal	1:1,000	Alexa 594	ICC	Invitrogen
rabbit IgG	Goat	polyclonal	1:20,000	Alexa 680	WB	Invitrogen
mouse IgG	Goat	polyclonal	1:20,000	Alexa 680	WB	Invitrogen
Rabbit IgG	Donkey	polyclonal	1:20,000	IRDYE700DX	WB	Rockland

WB: Western Blotting
ICC: Immunocytochemistry

Nature Structural & Molecular Biology: doi:10.1038/nsmb.1621

SUPPLEMENTARY DISCUSSION

Mutations in the IST1 α5-core interface inhibit cytokinesis and redistribute the protein to the insoluble/membrane-bound fraction

Truncated ESCRT-III proteins that lack autoinhibition typically redistribute, together with other ESCRT-III subunits, into "trapped" membrane-bound complexes. Such constructs are typically inactive and, indeed, often dominantly inhibit normal ESCRT-III functions (e.g., refs. [2,3]). As discussed in the main text, mutations that destabilize the interface between the autoinhibitory α5 helix and the core can constitutively activate CHMP3 proteins for assembly and inhibition of HIV-1 budding. We therefore tested whether analogous mutations in IST1 would also inhibit abscission and redistribute IST1 into the insoluble membrane-bound/assembled fraction of cell lysates.

We performed analyses of IST1 abscission functions by depleting endogenous IST1[4] and then testing the ability of siRNA-resistant IST1 constructs to rescue the midbody arrest (Supplemental Fig. 4). Three different IST1 mutant proteins were tested in these experiments ($IST1_{I60D}$, $IST1_{I169D}$, and the double mutant $IST1_{I60D, L166D}$). Each of these proteins harbored a different mutation that was predicted to disrupt the interface between the autoinhibitory α5 helix and the core α2 helix (see Supplemental Fig. 4a). As expected, siRNA depletion of endogenous IST1 increased the percentage of HeLa cells with visible midbodies from 4±1% to 20±3% (Supplemental Fig. 4b, compare lanes 1 and 2 and Supplemental Fig. 4c, panels 1 and 2). The midbody arrest defect was largely (though not entirely) rescued by re-expression of a wild type, siRNA-resistant IST1 construct (8±2%, lane/panel 3,

Nature Structural & Molecular Biology: doi:10.1038/nsmb.1621

positive control). In contrast, none of the mutant IST1 proteins rescued the midbody arrest to any significant extent, and the percentages of HeLa cells with visible midbodies ranged from 17-22%, which was not appreciably different from IST1-depleted cells treated with the empty vector control. We therefore conclude that disruption of the interface between the autoinhibitory α5 helix and the core α2 helix inactivates IST1 abscission functions.

ESCRT-III proteins cycle between soluble and membrane-bound/assembled states, and ESCRT-III partitioning assays have been used to detect enrichment of post-translational modifications in the assembled state[5], disassembly of membrane-bound ESCRT-III complexes by VPS4 enzymes[5-7], altered protein interactions in assembled vs. soluble states[8], and release of ESCRT-III autoinhibition by C-terminal protein truncations[3]. We employed the partitioning assay to test whether the α5-α2 interface mutants caused IST1 to be enriched in the insoluble membrane-bound/assembled fraction of cell extracts, as would be expected if this mutation constitutively activates IST1. As shown in the western blots in Supplemental Fig. 4b, both endogenous and exogenous wild type IST1 proteins partitioned between the soluble and insoluble fractions, but the bulk of these proteins were in the soluble fraction (lanes 1 and 3, compare upper and lower panels, 42% and 30% insoluble, respectively). In contrast, all three of the α5-α2 mutations dramatically repartitioned IST1 into the insoluble fraction (lane 4-6, 85-95% insoluble). Thus, mutations predicated to disrupt binding of the autoinhibitory helix to the core repartitioned IST1 toward the membrane-bound/assembled state *in vivo*.

Nature Structural & Molecular Biology: doi:10.1038/nsmb.1621

The experiments presented above are all consistent with the idea that α5-α2 mutations may function by relieving IST1 autoinhibition and thereby activate IST1 for membrane binding and assembly. However, IST1 autoinhibition and activation has not been documented, and we note that there are alternative possible explanations for the data because the IST1 α5-α2 mutations all block CHMP1B binding (which could explain the loss of abscission functions) and it is possible that the mutations simply reduce protein solubility by inducing IST1 to sample a non-native protein conformation (which could explain the repartitioning of these mutants into the membrane-bound/insoluble fraction). Hence, our experiments support the idea that IST1 can be activated by disruption of the α5-α2 interface, but do not prove this model.

Nature Structural & Molecular Biology: doi:10.1038/nsmb.1621

SUPPLEMENTARY METHODS

Protein expression and purification. We expressed CHMP3, $CHMP3_{8-222}$, $CHMP3_{1-150}$, $CHMP3_{V48D,\ A64D}$, $CHMP3_{V59D,\ V62D,\ I168D,\ L169D}$, $CHMP3_{I168D,\ L169D}$ and CHMP1B proteins with N-terminal GST affinity tags in BL21 (RIPL) *E. coli* grown in auto-induction media ZYP-5052[9] (3 L cultures for CHMP3 proteins, 6 L cultures for CHMP1B). Cells were grown at 37 ºC for 6 hours with vigorous shaking in baffled flasks before moving to 23 ºC and growing to saturation for 16-18 hours. Subsequent purification steps were performed at 4 ºC and were the same for all proteins except where specified. Cells were lysed with sonication, lysozyme and sodium deoxycholate treatment (50 mM Tris pH 7.0, 300 mM NaCl, 5 mM β-mercaptoethanol (BME)), and the supernatant was clarified by low speed centrifugation. 0.1 equivalent (v:v) of 10% polyethyleneamine (PEI) in 0.2 M NH_4SO_4 was added and nucleic acid precipitates were removed by centrifugation. The clarified supernatant was dialysed for 12 h against glutathione column loading buffer (10 mM potassium phosphate, pH 7.4, 150 mM NaCl, 5 mM BME), filtered, and applied to a Glutathione Sepharose 4 Fast Flow column (GE Healthcare) at 0.5 ml min^{-1}. The bound protein was washed extensively with loading buffer, and eluted with 50 mM Tris, pH 8.0, 150 mM NaCl, 20 mM reduced glutathione, 5 mM BME. The eluted protein (~70 ml) was dialyzed against 50 mM Tris, pH 8.0, 50 mM NaCl, 5 mM BME while incubating with TEV protease (0.6 mg per 70 ml) to remove the GST tag (12 h for CHMP3 proteins, 24 h for CHMP1B, 23 ºC). The processed protein was dialyzed against SP column loading buffer (25 mM Tris, pH 6.5, 150 mM NaCl, 5 mM BME), applied to a SP Sepharose Fast Flow column (GE Healthcare),

Nature Structural & Molecular Biology: doi:10.1038/nsmb.1621

and washed with loading buffer before elution with a gradient from 150 mM NaCl to 1 M NaCl in 25 mM Tris, pH 8.0, 5 mM BME. For CHMP3 proteins, residual GST was removed by an additional pass through a Glutathione Sepharose 4 Fast Flow Resin column. Finally, monomeric CHMP3 and CHMP1B proteins were separated from aggregates by gel filtration chromatography in 10 mM Tris, pH 8.0, 100 mM NaCl, 5 mM BME on a HiLoad 16/60 Superdex S75 column (GE Healthcare). Yields were ~30 mg for the wild type CHMP3 protein (3 L cultures) and ~1 mg CHMP1B (6 L culture), and the proteins could be concentrated to up to 30 mg ml^{-1} (CHMP3) or ~1 mg ml^{-1} (CHMP1B) in gel filtration buffer.

We expressed CHMP2A as a GST fusion, lysed (50 mM potassium phosphate, pH 7.2, 200 mM NaCl, 1 mM DTT) and purified as described for the CHMP3 proteins except for the following modifications: 1) The protein was precipitated from clarified lysate following the 10% PEI treatment by addition of 0.4 equivalents (v:v) saturated ammonium sulfate solution. The pellet was then dissolved in lysis buffer and applied to a Glutathione Sepharose 4 Fast Flow column. 2) After TEV treatment, the processed protein was dialyzed against Q column loading buffer (50 mM Tris, pH 8.0), applied to a Q Sepharose Fast Flow column (GE Healthcare) and washed with loading buffer before elution with a gradient from 0 to 250 mM NaCl in 50 mM Tris, pH 8.0. 3) Monomeric CHMP2A protein was separated from aggregates by gel filtration chromatography in 10 mM Tris pH 8.0, 100 mM NaCl, 1 mM DTT on a HiLoad 16/60 Superdex S75 column (GE Healthcare). This procedure typically yielded 45 mg CHMP2A from 6 L cultures and CHMP2A could be concentrated to 20 mg ml^{-1} in gel filtration buffer.

Nature Structural & Molecular Biology: doi:10.1038/nsmb.1621

We expressed $IST1_{NTD}$ as a GST fusion, lysed (50 mM Tris pH 8.0, 1 M NaCl, 5% (v/v) glycerol, 5 mM BME) and purified as described for the CHMP3 proteins except for the following modifications: 1) The clarified, filtered supernatant was applied directly (without PEI treatment) to a Glutathione Sepharose 4 Fast Flow column (GE Healthcare) at 0.5 ml. min^{-1} and eluted with 50 mM Tris, pH 8.0, 1 M NaCl, 5% (v/v) glycerol, 20 mM reduced glutathione, 5 mM BME. 2) The eluted protein was dialysed against 50 mM Tris, pH 8.0, 250 mM NaCl, 1 mM DTT while incubating with TEV protease (0.4 mg per 40 ml, 24 hours, 23 °C). 3) The processed protein was dialysed for 12 hours against SP column loading buffer (50 mM Tris, pH 7.0, 150 mM NaCl, 5% (v/v) glycerol, BME), applied to a SP Sepharose Fast Flow column (GE Healthcare) and washed with loading buffer before elution with a gradient of 150 mM to 1 M NaCl in 50 mM Tris, pH 7.0, 5% (v/v) glycerol, 5 mM BME. 4) Monomeric $IST1_{NTD}$ was separated from aggregated species by gel filtration chromatography in 50 mM Tris pH 7.0, 350 mM NaCl, 5% (v/v) glycerol, 1 mM DTT on a HiLoad 16/60 Superdex S75 column (GE Healthcare). This procedure typically yielded 30 mg $IST1_{NTD}$ from 4 L cultures and the protein could be concentrated to 15 mg ml^{-1} in gel filtration buffer.

Biosensor binding assays. We performed Biosensor binding experiments as previously reported using BIACORE2000 and 3000 instruments[10]. Briefly, GST-$IST1_{NTD}$ proteins were expressed and captured directly from BL21 (DE3) codon+ (RIPL) *E. coli* extracts onto anti-GST antibody-derivatized CM5 sensor chips. Purified CHMP1B protein was diluted at the designated concentrations in binding

Nature Structural & Molecular Biology: doi:10.1038/nsmb.1621

buffer (10 mM Tris (pH 8.0), 100 mM NaCl, 1 mM DTT, supplemented with 0.01% (v/v) Tween-20 and 0.2 mg ml^{-1} BSA), injected in triplicate (50 μL per min, 20°C) and binding data were collected at 2 Hz during the 12-30 second association and dissociation phases (Fig. 4a). The biosensor studies were complicated by the tendency of CHMP1B to bind non-specifically to the sensor chip, but this problem was minimized by keeping the CHMP1B analyte concentration below 20 μM, by subtracting the responses from a reference surface with GST alone, and in some cases by limiting the CHMP1B contact time to 12 seconds. All interactions reached equilibrium rapidly and dissociated within seconds during the dissociation phase. Dissociation constants were obtained by fitting the equilibrium responses to 1:1 binding models.

ESCRT-III assembly reactions. We performed assembly reactions as described below, and the resulting complexes were analyzed by TEM with negative staining.

$IST1_{NTD}$ was diluted from concentrated stocks in high salt buffer (350 mM NaCl, 50 mM Tris pH 7, 5% (v/v) glycerol, 1mM DTT) into equivalent buffers that contained either 100 mM NaCl or 350 mM NaCl. Assembly at 23 °C was followed in real time by light scattering at 330 nm (Fig. 6a).

CHMP1B was assembled by dialyzing the protein for 12 h into 30 mM NaCl, 10 mM Tris, pH 8.0, 1 mM DTT at a final protein concentration of 40 μM (4 ºC).

We co-assembled pure recombinant monomeric CHMP2A and CHMP3 proteins by incubating mixtures of the two proteins at 23 ºC for 30 min. Assembly conditions

Nature Structural & Molecular Biology: doi:10.1038/nsmb.1621

were surveyed over a range of ionic strengths (0-100 mM NaCl, 25 mM Tris pH8.0, 5 mM β-mercaptoethanol), molar protein ratios (0.5-2), and final protein concentrations (50-120 μM). Reactions containing isolated CHMP2A or CHMP3, mixtures of full length CHMP2A+CHMP3, and mixtures of CHMP2A+CHMP3$_{V59D,\ V62D,\ I168D,\ L169D}$ did not assemble into regular structures under any conditions tested, mixtures of CHMP2A+CHMP3$_{1-150}$ and of CHMP2A+CHMP3$_{I168D,\ L169D}$ assembled under all conditions tested, and mixtures of CHMP2A+CHMP3$_{V48D,\ A64D}$ assembled under the higher protein (≥100 μM) and salt (≥50 mM NaCl) conditions. Assembly conditions for the images shown in Fig. 7 were: a) CHMP2A (120 μM)+CHMP3 (120 μM) in 0 M NaCl, b) CHMP2A (50 μM)+CHMP3$_{1-150}$ (50 μM) in 0 M NaCl, c) CHMP2A (120 μM)+CHMP3$_{V48D,\ A64D}$ (120 μM) in 50 mM NaCl, d) CHMP2A (120 μM)+CHMP3$_{I168D,\ L169D}$ (120 μM) in 0 M NaCl, e) CHMP2A+CHMP3$_{V59D,\ V62D,\ I168D,\ L169D}$ (120 μM) in 100 M NaCl.

GST pulldown assays. We induced 5ml *E. coli* cultures to express GST-CHMP3 proteins using the autoinduction method, pelleted and lysed them by treatment (4°C, 20 minutes) with 1 mg ml^{-1} lysozyme in 4 ml binding buffer (10 mM Tris-HCl (pH 8.0), 100 mM NaCl, 5 mM β-mercaptoethanol, 5% (v/v) glycerol, 0.2% (v/v) NP40) followed by addition of 5% w/v sodium deoxycholate (4 °C, 20 minutes). Clarified lysates (1 ml) were incubated (1 h, 4°C) with 50 μl glutathione sepharose 4B matrix (pre-washed in binding buffer) followed by three binding buffer washes. Pure CHMP2A protein (35 μM in 1 ml binding buffer, ~5-fold molar excess over GST-CHMP3 proteins) was incubated with the GST-CHMP3/matrix for 1 hour at 4 °C and

Nature Structural & Molecular Biology: doi:10.1038/nsmb.1621

unbound proteins were removed by three binding buffer washes. Bound GST-CHMP3 and CHMP2A proteins were analyzed by boiling the matrices in 50 μl SDS loading buffer followed by Western blotting with anti-GST and anti-CHMP2A antibodies.

HIV-1 vector release and infectivity. We seeded 293T cells in 6-well plates at $5x10^5$ cells per well and co-transfected with pCAG-CHMP3-Myc expression constructs and an HIV-1 vector system (pCMVΔR8.2, pWPTS-nlsLacZ, phCMV-VSVG). Briefly, 8 μl Lipofectamine 2000 Transfection Reagent (Invitrogen) was combined with 1 μg pCMVΔR8.2, 1 μg pWPTS-nlsLacZ, 0.36 μg phCMV-VSVG, and 0.75 μg pCAG-CHMP3-Myc plasmid per well according to the manufacturer's instructions. Virions were harvested from the supernatant 24 hours post transfection, and analyzed for infectivity or pelleted through a 20% (w/v) sucrose cushion for western blotting. Cells were lysed in RIPA buffer for western blotting of intracellular proteins and visualized on an Odyssey scanner (LiCor Inc.). Vector titers were determined by transducing HeLa-M cells seeded in 96-well plates at $5x10^3$ cells per well.

IST1 partitioning assays. Transfected HeLa-M cells were harvested, washed in PBS, and resuspended in 50 μl lysis buffer (10 mM sodium phosphate, 400 mM KCl, 10% (v/v) glycerol, supplemented with protease inhibitors). Cells were lysed by three freeze thaw cycles, and the soluble supernatant was collected following centrifugation at 13,000 x g for 30 min at 4 °C ("Soluble Fraction"). To prepare the

Nature Structural & Molecular Biology: doi:10.1038/nsmb.1621

insoluble fractions, pellets were washed once by resuspension in 100 µl lysis buffer, recentrifuged, and solubilized in 100 µl 2X SDS-PAGE buffer ("Insoluble, Assembled/Membrane Bound Fraction"). Normalized levels of both soluble and insoluble fractions were loaded. Proteins were analyzed by Western blotting using a rabbit anti-IST1 antibody[4] and developed using a secondary Alexa 680-conjugated goat anti-rabbit antibody. Protein partitioning levels were quantified using an Odyssey Infrared Imaging System (Li-Cor).

Nature Structural & Molecular Biology: doi:10.1038/nsmb.1621

SUPPLEMENTARY REFERENCES

1. Group, C.C.P. The CCP4 Suite:Programs for Protein Crystallography. *Acta Crystallogr D50* **50**, 760-763 (November 4. 1994).

2. Zamborlini, A. et al. Release of autoinhibition converts ESCRT-III components into potent inhibitors of HIV-1 budding. *Proc Natl Acad Sci U S A* **103**, 19140-5 (2006).

3. Shim, S., Kimpler, L.A. & Hanson, P.I. Structure/function analysis of four core ESCRT-III proteins reveals common regulatory role for extreme C-terminal domain. *Traffic* **8**, 1068-79 (2007).

4. Bajorek, M. et al. Biochemical Analyses of Human IST1 and Its Function in Cytokinesis. *Mol Biol Cell* (2009).

5. von Schwedler, U.K. et al. The protein network of HIV budding. *Cell* **114**, 701-13 (2003).

6. Babst, M., Wendland, B., Estepa, E.J. & Emr, S.D. The Vps4p AAA ATPase regulates membrane association of a Vps protein complex required for normal endosome function. *Embo J* **17**, 2982-93. (1998).

7. Yoshimori, T. et al. The mouse SKD1, a homologue of yeast Vps4p, is required for normal endosomal trafficking and morphology in mammalian cells. *Mol Biol Cell* **11**, 747-63. (2000).

8. Shim, S., Merrill, S.A. & Hanson, P.I. Novel Interactions of ESCRT-III with LIP5 and VPS4 and their Implications for ESCRT-III Disassembly. *Mol Biol Cell* **19**, 2661-72 (2008).

9. Studier, F.W. Protein production by auto-induction in high density shaking cultures. *Protein Expr Purif* **41**, 207-34 (2005).

10. Stuchell-Brereton, M.D. et al. ESCRT-III recognition by VPS4 ATPases. *Nature* **449**, 740-4 (2007).

Nature Structural & Molecular Biology: doi:10.1038/nsmb.1621